Artificial Intelligence-Based Modeling and Control Strategy for Dual Active Bridge Converter With Triple Phase Shift Modulation

Jiawei Zhang, Jiaxiong Xu, Yile Dai, Miao Yu, *Member, IEEE*, Xin Zhang, *Senior Member, IEEE*, and Huai Wang, *Senior Member, IEEE*

***Abstract*—Dual active bridge (DAB) converter, known for its exceptional performance in bidirectional power transmission, has emerged as a crucial power conversion unit in energy storage systems and dc power systems. To improve the efficiency under wide voltage variations, the triple phase shift (TPS) modulation is typically used. However, the existing analytical models and control strategies of DAB with TPS modulation mostly depend on complex theoretical derivations, neglecting nonideal factors or exhibit heavy computational burdens. To tackle this issue, an artificial intelligence (AI)-based modeling and control strategy is proposed. First, a numerical simulation model incorporating the dynamic behavior of DAB circuit during dead time and parasitic parameters is developed to efficiently generate the training dataset. Building upon this, a general AI model of TPS modulation is precisely formulated, which is concise and applicable to various circuit parameters and all switching modes. Subsequently, a multilayer heuristic algorithm is employed to effectively derive optimal steady-state strategies. In addition, a concise artificial neural network is constructed to fit the offline control law and generate the optimal strategies online. Furthermore, an adaptive neural network sliding mode controller is designed. It integrates the general AI model with nonlinear sliding mode control theory, while a recurrent neural network compensates for errors adaptively, exhibiting excellent robustness and transient performance. Finally, comparative experiments demonstrate the effectiveness and superiority of the proposed approach.**

***Index Terms*—Dual active bridge (DAB), general artificial intelligence (AI) model, recurrent neural network (RNN), sliding mode control (SMC), triple phase shift (TPS).**

I. Introduction

DUE to the exceptional performance in bidirectional power transmission, high-frequency current isolation, and wide voltage range, the dual active bridge (DAB) dc–dc converter [1] has found extensive applications in energy storage systems, dc grids, and renewable energy sector. However, the frequent fluctuations in operating conditions and external uncertainty render the safe and efficient operation of DAB converters a challenging task.

Various modulation techniques [2] are developed to improve the operating performance of DAB, among which the single phase shift (SPS) [3] is the most fundamental method. Each switch with SPS modulation can achieve zero-voltage switching (ZVS) [4] when the voltage gain is unity. However, under wide voltage variations, it faces great challenges, such as difficulties in achieving ZVS, high ripple currents, and inefficiency. Consequently, triple phase shift (TPS) modulation [5] with three degrees of freedom has emerged, which enables lower current stress, wider ZVS range, and higher transmission efficiency. Nevertheless, this modulation relies on more complex modeling and control strategies.

Currently, the main modeling theories for DAB converters with TPS modulation primarily include the linear piecewise time-domain model [6] and the harmonic analysis method [7], [8]. The former relies on complex theoretical derivations, and fails to yield a unified expression applicable to all switching modes of DAB with TPS modulation. While the latter exhibits high-order nonlinearity, which makes it challenging to embed within the transient controller.

In response to the defects of above modeling theories, the artificial intelligence (AI)-based modeling approach [9] has emerged due to its high accuracy. For instance, a time-domain analytical model based on recurrent neural network (RNN) has been proposed in [10], which exhibits excellent on-call prediction capability. In addition, in [11], an AI-based design with data trimming is proposed to precisely model the current stress of DAB. Considering parasitic parameters, a nonideality inclusive frequency domain model (NIFDM) coupled with a physics-informed neural network is constructed in [12], thus facilitating accurate estimation of inductor current and converter losses. Nonetheless, these models exhibit high complexity, making them unsuitable for conventional microprocessors and transient control strategies design. Consequently, there is an urgent demand to develop a general analytical model for DAB with TPS modulation, which needs to be concise and without complex theoretical derivation.

Received 5 March 2025; revised 21 June 2025; accepted 24 July 2025. Date of publication 31 July 2025; date of current version 22 October 2025. This work was supported by the Fundamental Research Funds for the Central Universities under Grant 226-2024-00244. Recommended for publication by Associate Editor A. Dekka. *(Corresponding author: Miao Yu.)*

Jiawei Zhang, Jiaxiong Xu, Yile Dai, Miao Yu, and Xin Zhang are with the College of Electrical Engineering, Zhejiang University, Hangzhou 310027, China, and also with the Zhejiang Key Laboratory of Electrical Technology and System on Renewable Energy, Hangzhou 310027, China (e-mail: 22310056@zju.edu.cn; 12310011@zju.edu.cn; 22460290@zju.edu.cn; zjuyumiao@zju.edu.cn; zhangxin_ieee@zju.edu.cn).

Huai Wang is with AAU Energy, Aalborg University, 9200 Aalborg, Denmark (e-mail: hwa@et.aau.dk).

Color versions of one or more figures in this article are available at https://doi.org/10.1109/TPEL.2025.3594613.

Digital Object Identifier 10.1109/TPEL.2025.3594613

Apart from the challenges posed by modeling, DAB converters also suffer from steady-state efficiency problems and transient performance issues. For the optimization of steady-state efficiency, current stress [13], rms current of the inductor [14], [15], [16], and reactive power [17] are typically selected as objective functions. The soft switching operation [18] is usually treated as a constraint. For nonideal DAB converters, dead time and parasitic capacitance are considered in [19], but it still uses conventional linear piecewise models while neglecting the nonlinearity of parasitic parameters, leading to the possibility of soft switching misjudgment. To achieve optimal steady-state control online, traditional methods mostly rely on lookup tables. However, these approaches place higher demands on the speed and memory size of the microprocessor. Besides, it is difficult to ensure the optimality of the strategy. Therefore, online optimizers, such as reinforcement learning (RL) and artificial neural networks (ANN) [20], have been applied. Despite this, such steady-state optimizers currently exhibit complex network structures and long computational time.

On the other hand, in TPS modulation, studies aimed at enhancing transient performance are relatively few compared to that for steady-state optimization. Some linear control techniques, such as proportional integral control (PI), feedforward control [21], and dual-loop fault tolerant control [22], [23], have been introduced to enhance the dynamic behavior. However, the performance of linear controllers may degrade due to the inherent nonlinearity in the system. In response, nonlinear control strategies, such as model predictive control (MPC) [24], [25], fast boundary control [26], and sliding mode control (SMC) [27], have been proposed. Nevertheless, they generally require complex theoretical derivations and lack a unified expression tailored for all switching modes of DAB with TPS modulation. Thus, most of these advanced control strategies are used in the SPS modulation, while only a few have been applied in the TPS modulation. For example, to minimize output voltage tracking error and improve system operation efficiency simultaneously, an MPC approach was applied to TPS control in [28]. However, the accuracy of the model significantly influences the control performance, and the optimal strategy is difficult to attain.

In recent years, AI has attracted considerable attention in the control of power electronics. However, its application in DAB controller has focused predominantly on steady-state optimization [29], [30], [31]. The AI-based transient control methods are mostly restricted to simple SPS modulation. For instance, ANNs were employed in [32] to adaptively adjust controller parameters, which can achieve excellent transient performance without the need for current sensors. Similarly, a deep RL-based controller was proposed in [33] and [34] to achieve a fast dynamic response with accurate voltage tracking. In [35] and [36], RNN was used for uncertainties estimation. Furthermore, in [37], an adaptive weighting factor using ANN has been integrated into active disturbance rejection controller method to enhance disturbance rejection ability. However, due to the nonlinearity of the DAB model with TPS modulation, the design of AI-based strategies faces significant challenges. The high complexity and heavy computational burden may hinder their implementation in practice.

Addressing the limitations of existing modeling and control methods, this article proposes an AI-based strategy for DAB with TPS modulation. Through the combination of the numerical simulation results and the ANN structure, a general AI model is constructed, which has a concise expression and enjoys high accuracy. The numerical simulation comprehensively accounts for the influence of parasitic parameters and effectively captures the circuit's dynamic behavior during dead time. Afterward, an AI-based controller is designed to significantly improve the system's transient performance and robustness, while simultaneously improving steady-state efficiency. The main contributions of this study are as follows.

1) A numerical simulation model is established to incorporate the dynamic behavior of the DAB circuit during dead time and parasitic parameters, enabling efficient generation of the training dataset. Furthermore, a general AI model of DAB with TPS modulation is developed without extensive theoretical derivations. It is applicable to various circuit parameters and all switching modes. In addition, its analytical expression is quite simple, making it easily integrated into the design of nonlinear controllers.
2) A steady-state optimizer that minimizes rms current and ensures soft switching operation is designed. During optimization, a multilayer heuristic algorithm is employed to obtain the optimal strategies. By employing ANN to fit the offline control laws, the optimizer can achieve online optimization while maintaining a low computational burden.
3) By integrating nonlinear control theory with the adaptive error compensation term based on RNN, an adaptive neural network sliding mode controller is designed. This controller demonstrates excellent transient performance and system robustness compared to others. More importantly, the proposed method is lightweight and easy to implement in practice.

The rest of this article is organized as follows. Section II presents a general description of DAB with TPS modulation. Section III shows the design process of the general AI model. Section IV details the controller for improving steady-state efficiency and transient performance. Section V showcases parameter design of the AI model and control strategies. Section VI presents the experimental results. Finally, Section VII concludes this article.

II. Analysis of DAB Converter With TPS Modulation

A. Introduction of TPS Modulation in DAB

Fig. 1 shows the DAB topology [38] and the typical operating waveforms under TPS modulation. C_1 and C_2 are the input and output capacitors, respectively. C_{oss} is the parasitic output capacitance of the SiC MOSFET. V_1 and V_2 represent the input and output voltages, respectively. The full bridge H_1 on the primary side and H_2 on the secondary side are connected through an inductor L_s and an isolation transformer, the turns ratio of the transformer is n. L_k represents the transformer leakage inductance. L_d and $R_{\rm eq}$ are the parasitic inductance and parasitic resistance, respectively. i_L is the inductor current. v_{ab} and v_{cd}

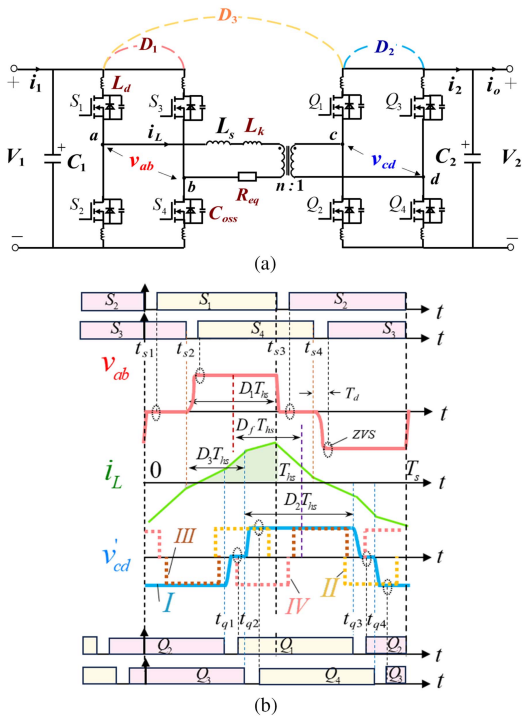

Fig. 1. TPS modulation of DAB converter. (a) DAB converter topotype. (b) Operating waveform of DAB with TPS modulation.

represent the voltage across the midpoint of the primary and secondary bridges, respectively. Therefore, the equivalent ac output voltage v'_{cd} of H_2 on H_1 side is equal to nv_{cd}. The voltage gain d can be defined as nV_2/V_1. T_s is the switching period, and T_{hs} represents the half period. T_d refers to the dead time.

In the TPS modulation, there are three degrees of freedom ($D_1, D_2,$ and D_3) to control the power flow and inductor current in DAB. D_1 and D_2 correspond to the inner phase shift ratios of H_1 and H_2, respectively. These inner phase shift ratios are designed to reduce reactive power and expand the ZVS range. D_3 represents the outer phase shift ratio between the output voltage v_{ab} of H_1 and the input voltage v_{cd} of H_2. In addition, D_f, which is defined as (1), represents the phase shift ratio between the fundamental components of v_{ab} and v'_{cd}

$$D_f = D_3 + \frac{D_2}{2} - \frac{D_1}{2}. \tag{1}$$

Moreover, the inner phase ratios D_1 and D_2 are within [0,1]. The direction of power flow is determined solely by D_f, thus, in scenarios involving forward power transmission and buck mode, $D_f > 0$. To simplify the analysis, we will focus on the operation scenario of the forward power transmission and the buck mode, and the other working conditions can be analyzed similarly.

B. Dynamic Behavior of the DAB Circuit During Dead Time

In practical applications, particularly at high frequencies, parasitic elements, such as C_{oss}, L_k, and L_d, play a crucial role in shaping the bridge-leg voltage and inductor current of the DAB converter. Thus, this section will analyze the dynamic behavior of the DAB circuit during the dead time while accounting for parasitic elements.

To ensure ZVS, sufficient energy must be stored in inductor to fully discharge or charge C_{oss} within a bridge leg during the dead time. This requires precise control of the inductor current and dead time. If the dead time is too short or the current in L_s and L_k is insufficient, then C_{oss} of the switch about to turn ON will not be fully discharged, resulting in incomplete ZVS (iZVS) or even hard switching. Conversely, an excessively long dead time will increase losses and may result in iZVS due to reresonance caused by the reversed current. Therefore, the conduction states of the switches can be broadly categorized into four types, as depicted in Fig. 2, including ZVS, iZVS due to short dead time or insufficient current, iZVS due to long dead time and reresonance, and hard switching.

Taking the ZVS process of S_4 as an example, the dynamic behavior of the DAB circuit during the dead time $[t_{s2}, t_{s2} + T_d]$ is analyzed as follows.

1) Stage 1—Before S_3 Turns OFF: Here, S_1 and S_3 are turned ON, keeping the voltage across the switches at zero. The impact of C_{oss} and L_d is negligible, so the equivalent circuit, as shown in Fig. 3(a), can be obtained. Thus, the dynamic equation of the inductor current before dead time is as follows:

$$(L_s + L_k)\frac{di_L(t)}{dt} = v_{ab}(t) - nv_{cd}(t) - R_{\text{eq}}i_L(t). \tag{2}$$

2) Stage 2—During the Resonance Between Inductance and C_{oss}: Once S_3 is turned OFF, the inductance and parasitic capacitance constitute a resonant circuit. During resonance, the inductor current is split into i_{off} and i_{on}, which charge the C_{oss} of S_3 and discharge the C_{oss} of S_4, respectively, until the voltage across S_4 drops to zero, as shown in Fig. 3(b). The sum of v_{ab} and the voltage across L_d associated with the conducting switch like S_1 is defined as v_{AB}. Accordingly, the following circuit state equations can be derived:

$$\begin{cases} i_L(t) = -i_{\text{off}}(t) + i_{\text{on}}(t) \\ L_d\frac{di_{\text{off}}(t)}{dt} = v_{AB}(t) - v_{\text{off}}(t) \\ L_d\frac{di_{\text{on}}(t)}{dt} = V_1 - v_{AB}(t) - v_{\text{on}}(t) \\ C_{oss}\left(v_{\text{off}}(t)\right)\frac{dv_{\text{off}}(t)}{dt} = i_{\text{off}}(t) \\ C_{oss}\left(v_{\text{on}}(t)\right)\frac{dv_{\text{on}}(t)}{dt} = i_{\text{on}}(t) \\ (L_s + L_k + L_d)\frac{di_L(t)}{dt} = v_{AB}(t) - nv_{cd}(t) - R_{\text{eq}}i_L(t) \end{cases} \tag{3}$$

where i_{off} and i_{on} represent the currents flowing through C_{oss} of S_3 and S_4, respectively. v_{off} and v_{on} are the drain–source voltages of the two switches.

Using the first-order Euler approximation, the state space variables mentioned above can be transformed into the following

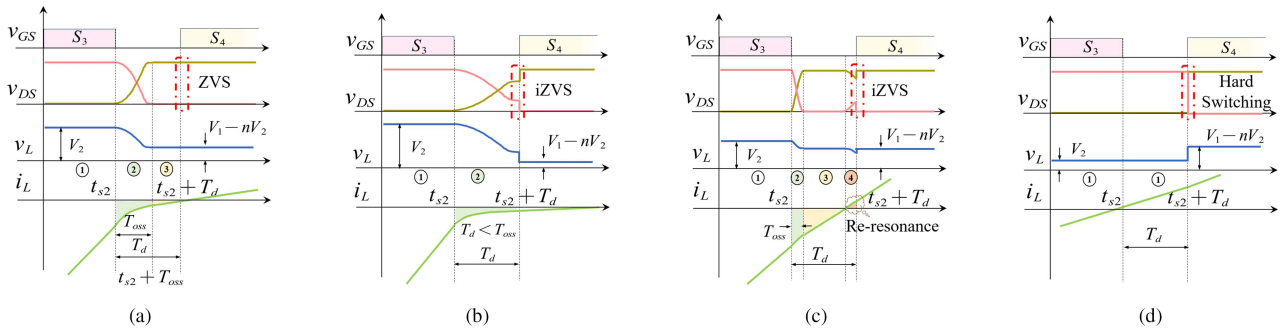

Fig. 2. Dynamic behavior of the DAB circuit within [0,T_d]. (a) ZVS. (b) iZVS under short dead time. (c) iZVS under long dead time. (d) Hard switching.

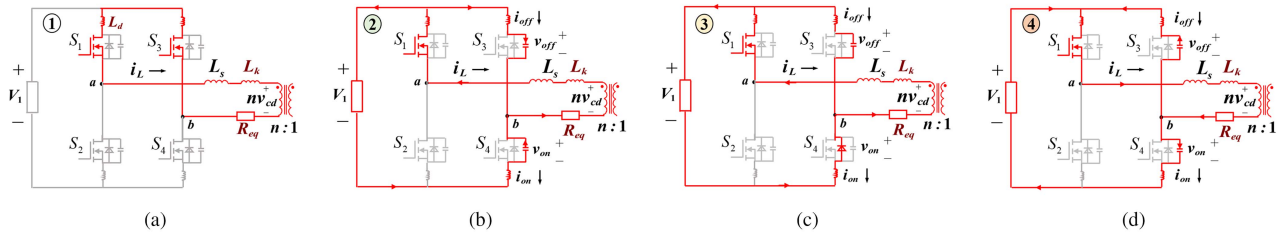

Fig. 3. Equivalent circuit of H_1 at different switching instant. (a) Equivalent circuit before t_{s2}. (b) Equivalent circuit within $[t_{s2}, t_{s2}+T_{oss}]$. (c) Equivalent circuit within $[t_{s2}+T_{oss}, t_{s2}+T_d]$. (d) Equivalent circuit when reresonance occurs.

difference equations:

$$\begin{cases} i_{\text{off}}[k+1] = & i_{\text{off}}[k] + \frac{\varphi_t}{L_d}\left((1-\iota_{s1})V_1 - \iota_{s2}v_{AB}[k]\right) \\ & -\frac{\varphi_t}{L_d}v_{\text{off}}[k] \\ v_{\text{off}}[k+1] = & v_{\text{off}}[k] + \frac{\varphi_t}{C_{oss}(v_{\text{off}}[k])}i_{\text{off}}[k] \\ v_{\text{on}}[k+1] = & v_{\text{on}}[k] + \frac{\varphi_t}{C_{oss}(v_{\text{on}}[k])}i_{\text{on}}[k] \\ v_{AB}[k+1] = & -\iota_{s1}\iota_{s2}V_1 + \iota_{s2}v_{\text{on}}[k+1] \\ & +\frac{\iota_{s2}L_d}{\varphi_t}\left(i_{\text{on}}[k]-i_{\text{on}}[k-1]\right) \\ i_L[k+1] = & i_L[k] + \frac{\varphi_t}{L_s+L_k+L_d} \\ & \times\left(v_{AB}[k] - nv_{cd}[k] - R_{\text{eq}}i_L[k]\right) \\ i_{\text{on}}[k+1] = & i_{\text{off}}[k+1] - \iota_{s2}i_L[k+1] \end{cases} \tag{4}$$

where φ_t represents the numerical simulation period. During the ZVS process before $S_1 - S_4$ turn ON, $[\iota_{s1}, \iota_{s2}]$ is equal to [0,-1], [0,1], [1,1], and [1,-1], respectively.

Such difference equations simplify the intricate task of solving differential equation systems into a straightforward sequential summation process, laying a solid foundation for the subsequent numerical modeling of the DAB circuit.

3) Stage 3—When the Antiparallel Diode Begins to Conduct: Once the drain–source voltage of S_4 discharges to 0 V, its antiparallel diode begins to conduct. Subsequently, v_{on} is clamped to zero, rendering the parasitic capacitance C_{oss} of S_4 negligible, as depicted in Fig. 3(c)

$$\begin{cases} i_{\text{off}}[k+1] = & i_{\text{off}}[k] + \frac{\varphi_t}{L_d}\left((1-\iota_{s1})V_1 - \iota_{s2}v_{AB}[k]\right) \\ & -\frac{\varphi_t}{L_d}v_{\text{off}}[k] \\ v_{\text{off}}[k+1] = & v_{\text{off}}[k] + \frac{\varphi_t}{C_{oss}(v_{\text{off}}[k])}i_{\text{off}}[k] \\ v_{AB}[k+1] = & -\iota_{s1}\iota_{s2}V_1 + \frac{\iota_{s2}L_d}{\varphi_t}\left(i_{\text{on}}[k]-i_{\text{on}}[k-1]\right) \\ i_L[k+1] = & i_L[k] + \frac{\varphi_t}{L_s+L_k+L_d} \\ & \times\left(v_{AB}[k] - nv_{cd}[k] - R_{\text{eq}}i_L[k]\right) \\ i_{\text{on}}[k+1] = & i_{\text{off}}[k+1] - \iota_{s2}i_L[k+1]. \end{cases}$$

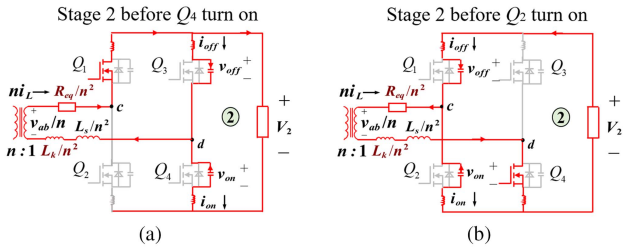

Fig. 4. Equivalent circuit of H_2 at stage 2. (a) Equivalent circuit within $[t_{q2}, t_{q2}+T_{oss}]$. (b) Equivalent circuit within $[t_{q3}, t_{q3}+T_{oss}]$.

4) Stage 4—When S_4 Turns ON With Complete ZVS: At the end of the dead time, the drain–source voltage of S_4 remains clamped to zero by the antiparallel diode, thereby ensuring complete ZVS.

For the reresonance phenomenon in Fig. 3(d), the circuit's dynamic equation remains consistent with (4) of stage 3.

Fig. 4 shows the equivalent circuit of DAB converter within $[t_{q2}, t_{q2}+T_{oss}]$ and $[t_{q3}, t_{q3}+T_{oss}]$. Analogous to (4), the difference equations for stage 2 during the switching transitions of H_2 can be derived. T_{oss} represents the resonance duration

$$\begin{cases} i_{\text{off}}[k+1] = & i_{\text{off}}[k] + \frac{\varphi_t}{L_d}\left((1-\iota_{q1})V_2 - \iota_{q2}v_{CD}[k]\right) \\ & -\frac{\varphi_t}{L_d}v_{\text{off}}[k] \\ v_{\text{off}}[k+1] = & v_{\text{off}}[k] + \frac{\varphi_t}{C_{oss}(v_{\text{off}}[k])}i_{\text{off}}[k] \\ v_{\text{on}}[k+1] = & v_{\text{on}}[k] + \frac{\varphi_t}{C_{oss}(v_{\text{on}}[k])}i_{\text{on}}[k] \\ v_{CD}[k+1] = & -\iota_{q1}\iota_{q2}V_2 + \iota_{q2}v_{\text{on}}[k+1] + \frac{\iota_{q2}L_d}{\varphi_t} \\ & \times\left(i_{\text{on}}[k] - i_{\text{on}}[k-1]\right) \\ i_L[k+1] = & i_L[k] + \frac{\varphi_t}{L_s+L_k+n^2L_d} \\ & \times\left(v_{ab}[k] - nv_{CD}[k] - R_{\text{eq}}i_L[k]\right) \\ i_{\text{on}}[k+1] = & i_{\text{off}}[k+1] + n\iota_{q2}i_L[k+1] \end{cases}$$

where, during the ZVS process before $Q_1 - Q_4$ turn ON, $[\iota_{q1}, \iota_{q2}]$ is equal to [0,-1], [0,1], [1,1], and [1,-1], respectively. Similarly, $v_{CD} = v_{cd} + v_{L_d}$, where v_{L_d} is the voltage across the parasitic inductance associated with the conducting switch (such as Q_1 during $[t_{q2}, t_{q2} + T_{oss}]$).

In summary, the dynamic behavior of the DAB converter during any switching transition can be readily derived from (2), (4), and (6).

C. General ZVS Constraints Considering Parasitic Parameters and Dead Time

Existing studies on ZVS constraints predominantly address energy limitations, with minimal consideration of the nonlinear effects of parasitic parameters and dead-time constraints. While Park et al. [19] incorporated dead-time constraints, its linear approximation of the switch's drain–source voltage v_{on} undermines the accuracy of the derived ZVS conditions. Therefore, this section will derive general ZVS constraints by considering the nonlinearities of parasitic parameters and state variables, as well as the constraints imposed by dead time.

1) Energy Constraints: To achieve complete ZVS during dead time, the energy stored in the inductor must be sufficient to discharge v_{on} to zero. For the ZVS process prior to S_4 turn-ON, the energy $Q_L = (L_s + L_k)I_{sg}^2/2$ stored in the inductor must meet the following constraint:

$$-\int_0^{T_{oss}} V_1 i_{\text{on}} dt + \int_0^{T_{oss}} n v_{cd} i_L dt + \int_0^{T_{oss}} i_L^2 R_{\text{eq}} dt + \int_0^{T_{oss}} v_{\text{off}} i_{\text{off}} dt + \int_0^{T_{oss}} v_{\text{on}} i_{\text{on}} dt < \frac{1}{2}(L_s + L_k) I_{sg}^2 \quad (7)$$

where $-I_{sg}$ denotes the initial value of i_L at the beginning of the dead time.

Based on the characteristics of the capacitor, the total energy absorbed by the C_{oss} of S_4 and S_3 can be expressed as

$$\begin{aligned}&\int_0^{T_{oss}} v_{\text{off}} i_{\text{off}} dt + \int_0^{T_{oss}} v_{\text{on}} i_{\text{on}} dt \\ &= \int_0^{V_1} v_{\text{off}} C_{oss}(v_{\text{off}})\, dv_{\text{off}} + \int_{V_1}^{0} v_{\text{on}} C_{oss}(v_{\text{on}})\, dv_{\text{on}} \\ &= 0. \end{aligned} \quad (8)$$

The energy absorbed by the parasitic resistance satisfies the following:

$$\int_0^{T_{oss}} i_L^2 R_{\text{eq}} dt < I_{sg}^2 R_{\text{eq}} T_{oss} \ll \frac{1}{2}(L_s + L_k) I_{sg}^2. \quad (9)$$

Moreover, combined with (4), the following equation can be derived:

$$\begin{aligned}&-\int_0^{T_{oss}} V_1 i_{\text{on}} dt + \int_0^{T_{oss}} n v_{cd} i_L dt \\ &= -\int_{V_1}^{0} V_1 dv_{\text{on}} C_{oss}(v_{\text{on}}) + \int_{V_1}^{0} n v_{cd} dv_{\text{on}} C_{oss}(v_{\text{on}}) \\ &\quad - \int_0^{V_1} n v_{cd} dv_{\text{off}} C_{oss}(v_{\text{off}}) \\ &= (V_1 - 2n v_{cd})\, Q_{oss}(V_1). \end{aligned} \quad (10)$$

Thus, the soft-switching constraint for the inductor current I_{sg} is given as

$$\sqrt{\frac{2(V_1 - 2n v_{cd})\, Q_{oss}(V_1)}{L_s + L_k}} < I_{sg}. \quad (11)$$

2) Dead-Time Constraints: Although sufficient energy is stored in the inductor, it may still fail to completely discharge the voltage v_{on} during the short dead time, resulting in iZVS. Therefore, the dead-time constraint must also be considered when analyzing ZVS conditions. To facilitate the modeling of the ZVS process, a linear charge-equivalent capacitance $C_{Q,\text{eq}}$ can be introduced, which exhibits the same amount of stored charge as the nonlinear capacitance [39] at a given drain–source voltage V_{DS}

$$C_{Q,eq}(V_{DS}) = \frac{Q_{oss}(V_{DS})}{V_{DS}} = \frac{\int_0^{V_{DS}} C_{oss}(v) dv}{V_{DS}}. \quad (12)$$

Thus, C_{oss} of the same bridge can be considered the same. Combining with (4), it can be derived that $i_{\text{on}} = -i_{\text{off}}$ and $i_{\text{on}} = -0.5\iota_{s2} i_L$. Subsequently, state variables i_{on}, i_L, and v_{on} of H_1 bridge during ZVS process satisfy

$$\begin{cases} \dot{v}_{\text{on}} = \frac{-\iota_{s2}}{2C_{Q,eq}(V_1)} i_L \\ \dot{i}_L = \frac{1}{L_s + L_k + 1.5L_d}(\iota_{s2} v_{\text{on}} - \iota_{s1}\iota_{s2} V_1 - n v_{cd}). \end{cases} \quad (13)$$

By extracting the constant coefficients from (13), the equation can be transformed into the following standard form:

$$\begin{cases} \dot{v}_{\text{on}} = \eta_{s1} i_L \\ \dot{i}_L = -\eta_{s2} v_{\text{on}} + \eta_{s2}\eta_{s3} \end{cases} \quad (14)$$

where $\eta_{s1}, \eta_{s2},$ and η_{s3} are constants corresponding to $S_1 - S_4$

$$\begin{cases} \eta_{s1} = \frac{-\iota_{s2}}{2C_{Q,eq}(V_1)} \\ \eta_{s2} = \frac{-\iota_{s2}}{L_s + L_k + 1.5L_d} \\ \eta_{s3} = \iota_{s1} V_1 + \iota_{s2} n v_{cd}. \end{cases} \quad (15)$$

Given $\eta_{s1}\eta_{s2} > 0$, if $\eta_{s2} > 0$, then the time-domain expressions of v_{on} and i_L can be obtained

$$\begin{cases} v_{\text{on}}(t) = & (V_1 - \eta_{s3}) \cos\left(\sqrt{\eta_{s1}\eta_{s2}}t\right) \\ & -I_{sg}\sqrt{\frac{\eta_{s1}}{\eta_{s2}}} \sin\left(\sqrt{\eta_{s1}\eta_{s2}}t\right) + \eta_{s3} \\ i_L(t) = & (\eta_{s3} - V_1)\sqrt{\frac{\eta_{s2}}{\eta_{s1}}} \sin\left(\sqrt{\eta_{s1}\eta_{s2}}t\right) \\ & -I_{sg} \cos\left(\sqrt{\eta_{s1}\eta_{s2}}t\right) \end{cases} \quad (16)$$

where I_{sg} should be positive to satisfy the energy constraint when $\eta_{s2} < 0$.

To facilitate the analysis of the monotonicity of $v_{\text{on}}(t)$, (16) can be rewritten as

$$\begin{cases} v_{\text{on}}(t) = \sqrt{\Upsilon_1^2 + \Upsilon_2^2} \cos\left(\sqrt{\eta_{s1}\eta_{s2}}t - \arctan\left(\frac{\Upsilon_2}{\Upsilon_1}\right)\right) \\ i_L(t) = \sqrt{\frac{\eta_{s2}(\Upsilon_1^2 + \Upsilon_2^2)}{\eta_{s1}}} \cos\left(\sqrt{\eta_{s1}\eta_{s2}}t + \arctan\left(\frac{\Upsilon_1}{\Upsilon_2}\right)\right) \end{cases} \quad (17)$$

where $\Upsilon_1 = V_1 - \eta_{s3}$ and $\Upsilon_2 = -I_{sg}\sqrt{\eta_{s1}/\eta_{s2}}$.

TABLE I
GENERAL ZVS CONSTRAINTS BY CONSIDERING PARASITIC PARAMETERS AND DEAD TIME

Condition	Conclusion	Energy Constraint I_E	Dead Time Constraint I_T	Constraint to Avoid Re-renonance I_R
S_1 turn ON (S_2 turn OFF)	$I_{sg1} < -I_{s1}^{zvs}$	$I_{Es1} = \sqrt{\frac{2(-V_1-2nv_{cd})Q_{oss}(V_1)}{L_s+L_k}}$	$I_{Ts1} = \eta_{s-}\frac{(V_1+nv_{cd})\cos\eta_{s+}-nv_{cd}}{\sin\eta_{s+}}$	$I_{Rs1} = -(nv_{cd}+V_1)\eta_{s-}\tan\eta_{s+}$
S_2 turn ON (S_1 turn OFF)	$I_{sg2} > I_{s1}^{zvs}$	I_{Es1}	I_{Ts1}	I_{Rs1}
S_4 turn ON (S_3 turn OFF)	$I_{sg4} < -I_{s4}^{zvs}$	$I_{Es4} = \sqrt{\frac{2(V_1-2nv_{cd})Q_{oss}(V_1)}{L_s+L_k}}$	$I_{Ts4} = \eta_{s-}\frac{nv_{cd}\cos\eta_{s+}+V_1-nv_{cd}}{\sin\eta_{s+}}$	$I_{Ts1} = -nv_{cd}\eta_{s-}\tan\eta_{s+}$
S_3 turn ON (S_4 turn OFF)	$I_{sg3} > I_{s4}^{zvs}$	I_{Es4}	I_{Ts4}	I_{Rs4}
Q_2 turn ON (Q_1 turn OFF)	$I_{qg2} < -I_{q2}^{zvs}$	$I_{Eq2} = \sqrt{\frac{2(2v_{ab}-nV_2)Q_{oss}(V_2)}{n(L_s+L_k)}}$	$I_{Tq2} = \eta_{q-}\frac{(V_2-v_{ab}/n)\cos\eta_{q+}+v_{ab}/n}{\sin\eta_{q+}}$	$I_{Tq2} = \left(\frac{v_{ab}}{n}-V_2\right)\eta_{q-}\tan\eta_{q+}$
Q_1 turn ON (Q_2 turn OFF)	$I_{qg1} > I_{q2}^{zvs}$	I_{Eq2}	I_{Tq2}	I_{Rq2}
Q_3 turn ON (Q_4 turn OFF)	$I_{qg3} < -I_{q3}^{zvs}$	$I_{Eq3} = \sqrt{\frac{2(2v_{ab}+nV_2)Q_{oss}(V_2)}{n(L_s+L_k)}}$	$I_{Tq3} = \eta_{q-}\frac{-(v_{ab}/n)\cos\eta_{q+}+V_2+v_{ab}/n}{\sin\eta_{q+}}$	$I_{Tq3} = \frac{v_{ab}}{n}\eta_{q-}\tan\eta_{q+}$
Q_4 turn ON (Q_3 turn OFF)	$I_{qg4} > I_{q3}^{zvs}$	I_{Eq3}	I_{Tq3}	I_{Rq3}

Note: $I_*^{zvs} = \max\{0, I_{E*}, I_{T*}, I_{R*}\}$, $\eta_{s-} = \sqrt{\frac{2C_{Q,eq}(V_1)}{L_s+L_k+1.5L_d}}$, $\eta_{s+} = \sqrt{\frac{1}{2C_{Q,eq}(V_1)(L_s+L_k+1.5L_d)}}$

$\eta_{q-} = \sqrt{\frac{2C_{Q,eq}(V_2)}{L_s+L_k+1.5n^2L_d}}$, $\eta_{q+} = \sqrt{\frac{n^2}{2C_{Q,eq}(V_2)(L_s+L_k+1.5n^2L_d)}}$

To prevent iZVS caused by reresonance, $i_L(t)$ must be less than zero at $t = t_{s2} + T_d$. Accordingly, the corresponding constraint is derived as

$$\frac{\pi}{2} < \sqrt{\eta_{s1}\eta_{s2}}T_d + \arctan\left(\sqrt{\frac{\eta_{s2}}{\eta_{s1}}}\frac{V_1-\eta_{s3}}{-I_{sg}}\right) < \frac{3\pi}{2}. \quad (18)$$

Therefore, the constraint of I_{sg} to avoid iZVS caused by reresonance can be expressed as

$$(\eta_{s3}-V_1)\sqrt{\frac{\eta_{s2}}{\eta_{s1}}}\tan\left(\sqrt{\eta_{s1}\eta_{s2}}T_d\right) < I_{sg}. \quad (19)$$

From (18), the following inequality is derived:

$$0 < \sqrt{\eta_{s1}\eta_{s2}}T_d + \arctan\left(\frac{\Upsilon_2}{\Upsilon_1}\right) < \pi. \quad (20)$$

That is to say that $v_{\rm on}(t)$ across the parasitic capacitance C_{oss} decreases monotonically during the dead time, provided that I_{sg} satisfies the energy constraint (11) and the constraint (20) to avoid reresonance. To achieve ZVS, i_L must discharge $v_{\rm on}$ to zero before the end of the dead time

$$\sqrt{\frac{\eta_{s2}}{\eta_{s1}}}\frac{(V_1-\eta_{s3})\cos\left(\sqrt{\eta_{s1}\eta_{s2}}T_d\right)+\eta_{s3}}{\sin\left(\sqrt{\eta_{s1}\eta_{s2}}T_d\right)} < I_{sg}. \quad (21)$$

During the dead time, before Q_2 and Q_3 turn ON, the dynamic equations of i_L and $v_{\rm on}$ are given as

$$\begin{cases}\dot{v}_{\rm on} = \eta_{q1}i_L \\ \dot{i}_L = -\eta_{q2}v_{\rm on} + \eta_{q2}\eta_{q3}\end{cases} \quad (22)$$

where η_{q1}, η_{q2}, and η_{q3} are constants corresponding to $Q_1 - Q_4$.

$$\begin{cases}\eta_{q1} = \frac{n\iota_{q2}}{2C_{Q,eq}(V_2)} \\ \eta_{q2} = \frac{n\iota_{q2}}{L_s+L_k+1.5n^2L_d} \\ \eta_{q3} = \iota_{q2}\frac{v_{ab}}{n} + \iota_{q1}V_2.\end{cases} \quad (23)$$

For $\eta_{q2} > 0$ during the dead time before Q_2 and Q_3 turn ON, the time-domain expressions of $v_{\rm on}$ and i_L, as well as the dead-time constraints, closely resemble those during the dead time before S_4 and S_1 turn ON. Based on the above analysis, the general ZVS constraints can be derived, as depicted in Table I, including the energy constraint, dead-time constraint, and the constraint to prevent iZVS caused by reresonance.

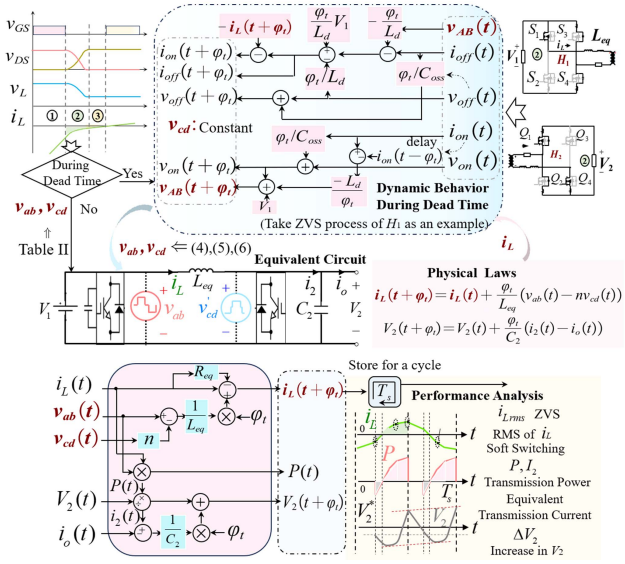

Fig. 5. Block diagram of numerical modeling based on physical laws of DAB.

III. AI-BASED MODELING OF DAB WITH TPS MODULATION

A. Numerical Modeling for DAB With TPS Modulation

Building AI model or intelligent control strategies requires a large training dataset. However, the data acquisition speed through traditional simulation software, such as MATLAB/Simulink, is very slow. Thus, this article proposes a numerical modeling method, which can rapidly acquire a large amount of data. The specific framework of the numerical simulation process is illustrated in Fig. 5.

Based on the equivalent circuit of DAB, as shown in Fig. 5, the dynamic equations of i_L, output voltage V_2, and transmission

TABLE II
TIME SERIES VALUES OF $v_{ab}(t), v_{cd}(t)$ AND ZVS CONSTRAINS FOR i_L WITHIN ONE CYCLE

Time series values of v_{ab}		General ZVS constrains	
$\omega_s t/2$	$v_{ab}(t)$	$\omega_s t/2$	$i_L(t)$
$[D_{td}, 1-D_1]$	0	$1-D_1$	$< -I_{s4}^{zvs}$
$[D_{td}+1-D_1, 1]$	V_1	1	$> I_{s1}^{zvs}$
$[D_{td}+1, 2-D_1]$	0	$1-D_1+D_3$	$> I_{q3}^{zvs}$
$[D_{td}+2-D_1, 2]$	$-V_1$	$(1-D_1+D_2+D_3) or (-1-D_1+D_2+D_3)$	$< -I_{q2}^{zvs}$
Time series values of v_{cd}			
$I.-D_1+D_3<0, -D_1+D_2+D_3>0$		$II.-D_1+D_3>0, -1-D_1+D_2+D_3<0$	
$\omega_s t/2$	$v_{cd}(t)$	$\omega_s t/2$	$v_{cd}(t)$
$[0, -D_1+D_2+D_3]$	$-V_2$	$[0, -D_1+D_3]$	0
$[D_{td}-D_1+D_2+D_3, 1-D_1+D_3]$	0	$[D_{td}-D_1+D_3, -D_1+D_2+D_3]$	$-V_2$
$[D_{td}+1-D_1+D_3, 1-D_1+D_2+D_3]$	V_2	$[D_{td}-D_1+D_2+D_3, 1-D_1+D_3]$	0
$[D_{td}+1-D_1+D_2+D_3, 2-D_1+D_3]$	0	$[D_{td}+1-D_1+D_3, 1-D_1+D_3+D_2]$	V_2
$[D_{td}+2-D_1+D_3, 2]$	$-V_2$	$[D_{td}+1-D_1+D_3+D_2, 2]$	0
$III.-D_1+D_2+D_3<0$		$IV.-1-D_1+D_2+D_3>0$	
$\omega_s t/2$	$v_{cd}(t)$	$\omega_s t/2$	$v_{cd}(t)$
$[0, 1-D_1+D_3]$	0	$[0, -D_1+D_2+D_3-1]$	V_2
$[D_{td}+1-D_1+D_3, 1-D_1+D_2+D_3]$	V_2	$[D_{td}-D_1+D_2+D_3-1, -D_1+D_3]$	0
$[D_{td}+1-D_1+D_2+D_3, 2-D_1+D_3]$	0	$[D_{td}-D_1+D_3, -D_1+D_2+D_3]$	$-V_2$
$[D_{td}+2-D_1+D_3, 2-D_1+D_2+D_3]$	$-V_2$	$[D_{td}-D_1+D_2+D_3, 1-D_1+D_3]$	0
$[D_{td}+2-D_1+D_2+D_3, 2]$	0	$[D_{td}+1-D_1+D_3, 2]$	V_2

current i_2 can be expressed as

$$\begin{cases} i_L(t+\varphi_t) = i_L(t) + \frac{\varphi_t}{L_{\text{eq}}}(v_{ab}(t) - n v_{cd}(t)) \\ i_2(t) = \frac{n i_L(t) v_{cd}(t)}{V_2(t)} \\ V_2(t+\varphi_t) = V_2(t) + \frac{\varphi_t}{C_2}(i_2(t) - i_o(t)) \end{cases} \tag{24}$$

where the equivalent capacitance $L_{\text{eq}} = L_s + L_k$.

From (24), to obtain the real-time values of $i_L(t+\varphi_t)$, the numerical values of v_{ab} and v'_{cd} within the time interval $[0, T_s]$ are needed. According to the switching sequences of two full bridges, v_{ab} has only one type within a switching cycle. In contrast, v'_{cd} presents four different waveform types, as shown in Fig. 1. Table II lists the numerical values of $v_{ab}(t)$ and $v_{cd}(t)$ within $[0, T_s]$, together with the constraints to achieve soft switching, $\omega_s = T_s$ and $D_{td} = 2T_d/T_s$. Outside the dead time, $v_{ab}(t)$ and $v_{cd}(t)$ are directly obtained from Table II, while during the dead time, their dynamic values are governed by (2), (4), and (6). Consequently, the dynamic waveform of $i_L(t)$ can be efficiently derived using this numerical modeling approach. This facilitates the rapid assessment of the rms of inductor current $i_{L\text{rms}}$, transmission power P, and the soft switching conditions of each switch.

The proposed numerical modeling approach eliminates complex theoretical derivations and low-order harmonic approximations, while greatly reducing the computational burden compared to other AI models, such as [10]. Consequently, this approach can provide substantial data for training the AI model and enable efficient evaluation of the modulation strategy for steady-state optimization.

B. General AI Model Using Feedforward Neural Network (FNN)

To tackle the absence of a lightweight and unified model for DAB with TPS modulation, a general AI model suitable for all switching modes and wide circuit parameters is first developed. This model can provide the theoretical foundation for the latter transient control strategies.

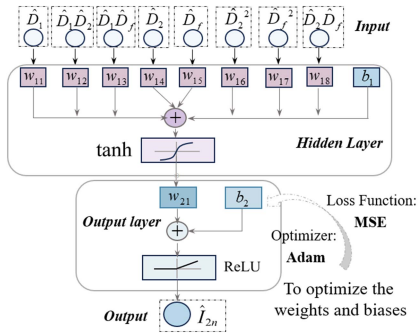

Fig. 6. Network diagram of the general AI model.

From (24), the output voltage $V_2[k+1]$ can be expressed as

$$V_2[k+1] = V_2[k] + \frac{T_c}{C_2}(I_2[k] - i_o[k]) \tag{25}$$

where T_c is the control cycle, equivalent transmission current $I_2[k]$ is the average value of i_2 over one switching cycle, $I_2 = P/V_2$, and k is the control instant.

It is apparent that if a general and simple relationship between I_2 and $\{D_1, D_2, D_f\}$ is established, a rapid and accurate regulation of V_2 can be achieved. This can be done through adjustment of the dynamic phase shift ratio.

Taking into account the exceptional fitting performance and the concise expression of ANN, a general AI model of I_2, presented in Fig. 6, is constructed. It is a three-layer FNN. In addition, the training dataset for the network comprises numerous numerical simulation results and a small amount of sampling data from the DAB prototype. In the following, D_1 is taken as the dynamic control variable to demonstrate the design process of the general AI model.

To simplify the subsequent design of the dynamic phase shift ratio D_1 during transient control, the hidden layer is configured with only one neuron. The input features are limited to contain merely first order of D_1. The activation functions for the hidden

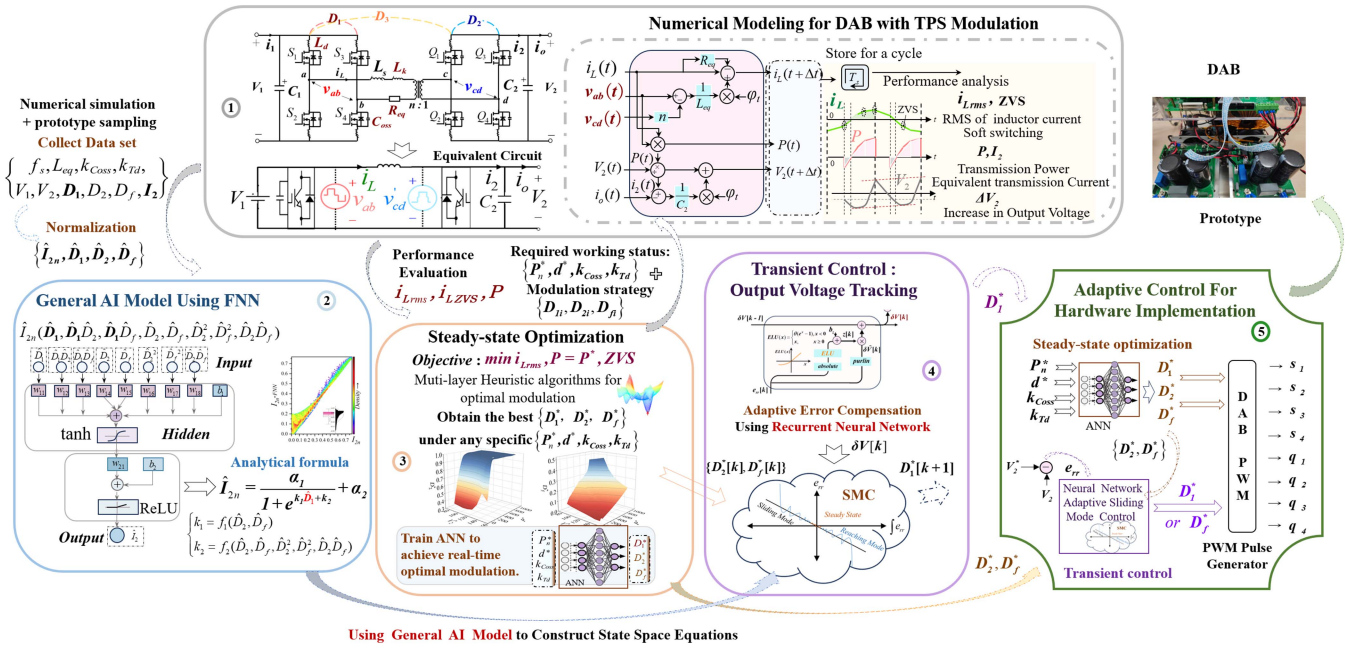

Fig. 7. Diagram of the proposed AI-based modeling and control of DAB converter.

layer and output layer are selected as tanh and rectified linear unit (ReLU), respectively. The expression of tanh is shown as follows:

$$\tanh(x) = \frac{2}{1+e^{-2x}} - 1. \tag{26}$$

Insufficient neurons in the hidden layer may inevitably lead to a low model accuracy. Consequently, several improvement measures have been implemented. For instance, I_2 is converted to I_{2n}, as shown in the following:

$$I_{2n} = I_2 \Big/ \left(\frac{nV_1}{2\pi L_{\mathrm{eq}} f_s}\right). \tag{27}$$

This modification can eliminate the impact of the operating conditions and circuit parameters on I_2. Furthermore, the original input $\{D_1, D_2, D_f\}$ is expanded to eight dimensions, represented as $\{D_1, D_1D_2, D_1D_f, D_2, D_f, D_2^2, D_f^2, D_2D_f\}$. These features are selected through an importance analysis using random forest.

Combining the connection weights w_{ij} and the bias parameters b_i of each neuron, we can derive the analytical expression of $\hat{I}_{2n}(\hat{D}_1, \hat{D}_2, \hat{D}_f)$ as

$$\hat{I}_{2n} = \frac{\alpha_1}{1+e^{k_1\hat{D}_1+k_2}} + \alpha_2 \tag{28}$$

where $\hat{I}_{2n}$ and $\{\hat{D}_1, \hat{D}_2, \hat{D}_f\}$ are the normalized values. k_1, k_2, α_1, and α_2 are the coefficients of the FNN model for $\hat{I}_{2n}$ of the DAB, which are described as

$$\begin{cases} k_1 = & -2(w_{11} + w_{12}\hat{D}_2 + w_{13}\hat{D}_f) \\ k_2 = & -2(w_{14}\hat{D}_2 + w_{15}\hat{D}_f + w_{16}\hat{D}_2{}^2 \\ & +w_{17}\hat{D}_f{}^2 + w_{18}\hat{D}_2\hat{D}_f + b_1) \\ \alpha_1 = & 2w_{21} \\ \alpha_2 = & -w_{21} + b_2. \end{cases} \tag{29}$$

From the analytical expression in (28), it can be inferred that the normalized dynamic phase shift ratio $\hat{D}_1$, $\hat{I}_{2n}$, and $\{\hat{D}_2, \hat{D}_f\}$ satisfy the following nonlinear relationship:

$$\hat{D}_1 = \frac{1}{k_1}\ln(\alpha_1/(\hat{I}_{2n} - \alpha_2) - 1) - \frac{k_2}{k_1}. \tag{30}$$

Similarly, when D_f serves as the dynamic control variable, we just need to replace D_1 with D_f in the aforementioned model.

IV. AI-Based Control Method for DAB

Fig. 7 shows the details of the AI-based scheme. In order to achieve enhancement of steady-state efficiency and transient performance, the AI-based controller consists of two parts. In the first part, D_2 and D_f are defined as static modulation ratios for light load, while D_1 and D_2 are for heavy load, both generated by an ANN fitting the optimal steady-state modulation laws. In another part, by using the general AI model and optimal static ratios, a transient controller based on SMC and RNN is constructed to generate the dynamic modulation ratio.

A. Steady-State Optimization for Minimum RMS Current With Soft Switching Operation

In the context of DAB with TPS modulation, $i_{L\mathrm{rms}}$ and soft switching conditions are often regarded as crucial performance indicators. Since D_f cannot achieve low power transmission at low voltage gain or with extended dead time, D_1 is chosen as the transient control variable under light load, while D_2 and D_f are set as static phase shift ratios. As the load increases and D_1 approaches saturation, D_f is then selected as the transient control variable under heavy load, with D_1 and D_2 set as static phase shift ratios. When formulating static phase ratios, the optimization objectives are to minimize $i_{L\mathrm{rms}}$. The constraint

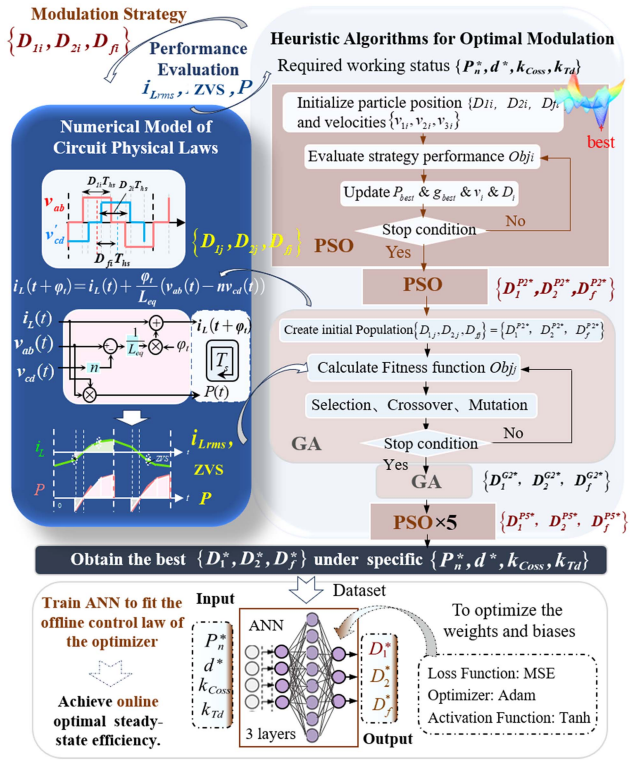

Fig. 8. Diagram of steady-state optimization for optimal static phase shift ratios.

is to ensure the soft switching operation, as shown in Table II, thereby achieving optimal steady-state efficiency. Then, a multilayer heuristic algorithm is designed to obtain the global optimal solution offline. Finally, in order to achieve online optimization, an ANN is trained to fit the offline control laws of the optimizer. The details of steady-state optimization are illustrated in Fig. 8.

To alleviate the computation burden, complex constraints, such as soft switching operation and power transmission, are incorporated into the objective function through the appliance of penalty functions [40]

$$\min Obj{=}i_{L\mathrm{rms}} + \rho\phi_{\mathrm{zvs}} + \beta(P - P^*)^2 \tag{31}$$

where ϕ_{zvs} represents the total number of switches that do not achieve ZVS, while ρ and β denote the ZVS and power penalty, respectively.

Subsequently, a multilayer heuristic algorithm is designed. It has excellent global search capabilities and rapid convergence rates. This algorithm consists of nine layers. The third and fourth layers implement genetic algorithm (GA), while the other layers utilize particle swarm optimization (PSO) algorithm. The optimal solutions obtained from the preceding layers are set as initial solutions for lower level algorithms. This approach ultimately generates the optimal modulation strategy $\{D_1^*, D_2^*, D_f^*\}$ for the specified conditions $\{P_n^*, d^*, k_{Coss}, k_{Td}\}$. k_{Coss} and k_{Td} represent the normalized parasitic capacitance and dead time, respectively. P_n^* denotes the normalized power, $P_n^* = P/(nV_1V_2/(2\pi f_s L_{\mathrm{eq}}))$, similar to (27).

The flowchart of the multilayer heuristic algorithm is shown in Fig. 8. Initially, the specific operating conditions $\{P_n^*, d^*, k_{Coss}, k_{Td}\}$ are given. The preliminary modulation strategy $\{D_{1i}, D_{2i}, D_{fi}\}$ is generated by the first PSO algorithm. This strategy is then substituted into the numerical model in Fig. 5. Such numerical simulation enables rapid assessment of the strategy performance by obtaining $i_{L\mathrm{rms}}$, P, and soft switching conditions. Then, the optimal individual strategy P_{best} and global strategy g_{best} are updated. The velocity v_i and strategy D_i are recalibrated according to the adjustment function. This iterative process continues until the convergence criteria are met.

Afterward, by traversing different operating conditions, an extensive dataset $\{P_n^*, d^*, k_{Coss}, k_{Td}, D_1^*, D_2^*, D_f^*\}$ of optimal modulation strategies can be obtained. Then, they are input into an ANN to fit the offline laws. The network is an FNN of three layers, with its weights and biases optimized by Adam. The trained neural network controller can generate the static phase shift ratios online for optimal steady-state efficiency in practice.

B. Transient Controller Based on Adaptive Neural Network SMC

Due to the excellent dynamic performance and robustness, SMC is widely employed in transient control strategies for nonlinear systems. Hence, this article utilizes SMC to establish a foundational framework for the transient controller under TPS modulation. Apart from this, RNN is employed as an adaptive error compensation term to enhance its ability to resist system uncertainties.

During the design of the transient controller, the goal is to track the output voltage V_2. The output voltage tracking error, indicated as e_{rr}, can be expressed as

$$e_{rr} = V_2^* - V_2. \tag{32}$$

Thus, the sliding surface s is designed as

$$s = \kappa_1 e_{rr} + \kappa_2 \int e_{rr} dt \tag{33}$$

where κ_1 and κ_2 are the proportional coefficients of the state variables on the sliding surface. Then, considering (24), the derivative of the sliding surface $\dot{s}$ can be obtained as

$$\dot{s} = \kappa_1 \dot{V}_2^* + \kappa_2 e_{rr} + \frac{\kappa_1}{C_2} i_o - \frac{\kappa_1}{C_2} I_2. \tag{34}$$

To prevent the chattering phenomenon when using the sgn function, the proposed SMC employs an exponential control law and replaces the original sgn function with the activation function tanh. Consequently, the control law for the sliding surface $\dot{s}$ is designed as

$$\dot{s} = -\delta_1 \tanh(\delta_3 s) - \delta_2 s \tag{35}$$

where δ_1, δ_2, and δ_3 are the parameters used to adjust the convergence rates.

In practice, the data-driven circuit model may not be completely accurate. Besides, there are numerous uncertainties associated with the circuit parameters and state variables. Therefore, relying solely on the aforementioned transient control strategy may lead to steady-state error of V_2 or poor system robustness.

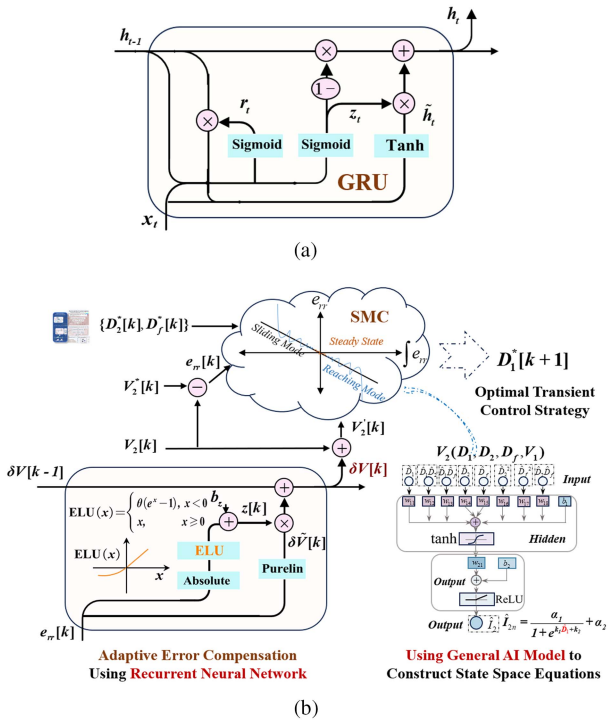

Fig. 9. Diagram of adaptive neural network sliding mode control. (a) Network architecture of GRU. (b) Diagram of error compensation term based on RNN.

The existing disturbance observers and other error compensation methods always rely on integral elements, which contain a time-sequenced summation of the error. Coincidentally, RNN has the ability to memory information from previous inputs and exhibits nonlinearity, which provides a novel approach for designing error compensation in nonlinear systems. Therefore, this article develops an adaptive error compensation term based on RNN, which can address the issue of slow convergence speed near the equilibrium state of traditional SMC. Thus, the steady-state error can be quickly eliminated.

Among the commonly used RNN, the gate recurrent unit (GRU) involves only a few linear transformations and nonlinear activation functions, making it more computationally efficient and simpler to implement. It consists mainly of two gating mechanisms: the update gate z_t and the reset gate r_t, as illustrated in Fig. 9(a).

Based on the structure of the GRU network, an adaptive compensation term for tracking error is designed in Fig. 9(b). $e_{rr}[k]$ is set as input. The new network does not include reset gate r_t. Thus, the mutual coupling effects between the previous state $\delta V[k-1]$ and the current input $e_{rr}[k]$ are omitted. In the error compensation method, the combination of the previous state $\delta V[k-1]$ and the current state $\delta\tilde{V}[k]$ differs from the time series prediction tasks. Consequently, in the newly established network, the weight of the previous state $\delta V[k-1]$ is set to 1, not $1-z[k]$. Similarly to GRU, the influence of the current state $\delta\tilde{V}[k]$ on the output state $\delta V[k]$ is governed by $z[k]$.

To improve the convergence rate of e_{rr} near the equilibrium state, two activation functions are designed between $e_{rr}[k]$ and $z[k]$. The previous one employs an absolute activation function, while the second utilizes the exponential linear unit (ELU) activation function, which is given as

$$\mathrm{ELU}(x)=\begin{cases}\theta(e^{x}-1), & x<0\\ x, & x\geq 0\end{cases} \tag{36}$$

where θ is a coefficient of the ELU. In addition, a positive bias b_z is introduced afterward to ensure $z[k]$ is positive. Meanwhile, the connection weight W_z is set to a negative value. This method allows the compensation to increase as the error decreases.

Given that a nonlinear term has already been incorporated into the update gate $z[k]$, Purelin is selected as the activation function between $e_{rr}[k]$ and $\delta\tilde{V}[k]$. Therefore, the adaptive error compensation term $\delta V[k]$ can be expressed as

$$\delta V[k]=\sum_{i=k_s}^{k} W_h e_{rr}[i]\cdot(\theta e^{W_z|e_{rr}[i]|}-\theta+b_z) \tag{37}$$

where k_s represents the moment when the output voltage error falls below the threshold $eV_{\min}$. W_z and W_h are the connection weights within network between $z_t, \tilde{h}_t$ and $[h_{t-1}, x_t]$, respectively.

By combining (28), (34), and (35), we can obtain the reference value of equivalent transmission current $I_2^*[k+1]$

$$I_2^*[k+1]=\frac{\delta_1\tanh(\delta_3 s)+\delta_2 s}{\kappa_1}C_2+C_2\dot{V}_2^*[k] +\frac{\kappa_2 C_2}{\kappa_1}(V_2^*[k]-V_2[k]-\delta V[k])+i_o[k] \tag{38}$$

where $V_2^*[k]$ is the reference output voltage. $\dot{V}_2^*[k]$ denotes the derivative of V_2^*. Considering the cost factors of the current sensor, we do not utilize the load current i_o in practical control, and $V_1[k]$ is replaced by a constant value $\tilde{V}_1$. Moreover, the controller has integrated an RNN-based error compensation term, which effectively mitigates the tracking error caused by the exclusion of i_o and V_1 in the final control. Then, $I_2^*[k+1]$ excluding i_o can be represented as $I_{2s}^*[k+1]$

$$I_{2s}^*[k+1]=\frac{\delta_1\tanh(\delta_3 s)+\delta_2 s}{\kappa_1}C_2+C_2\dot{V}_2^*[k] +\frac{\kappa_2 C_2}{\kappa_1}(V_2^*[k]-V_2[k]-\delta V[k]). \tag{39}$$

Next, by integrating I_{2s}^* of (39) into (30), the normalized optimal dynamic ratio $\hat{D}_1^*$ for the controller can be derived as

$$\hat{D}_1^*[k+1]=\frac{1}{k_1}\ln\left(\alpha_1\Big/\left(\frac{2\pi f_s L_{\mathrm{eq}}}{n\tilde{V}_1}\hat{I}_{2s}^*[k+1]-\alpha_2\right)-1\right) -\frac{k_2}{k_1}. \tag{40}$$

Similarly, when D_f serves as the dynamic control variable, we just need to replace D_1 with D_f in the aforementioned equation. Therefore, by combining δV with SMC, the proposed control method can improve both transient performance and robustness of the system. Furthermore, in practice, only the output voltage V_2 needs to be measured, eliminating the need for i_o and V_1.

TABLE III
PARAMETERS OF DAB CONVERTER

Parameters	Value
Inductance L_s	50 μH
Transformer	Turns ratio n 5/3 Leakage Inductance L_k 4 μH Pri. 500 turns Sec. 300 turns Litz wire 0.1 mm∗600 strands Core EC90.PC40
Output capacitance C_2	410 μF
Switching frequency f_s	100, 200 kHz
Switches	SiC MOSFET NTH4L040N120SC1
Input voltage V_1	200 − 400 V
Output voltage V_2	50 − 200 V
Transmission power P	0−600 W
Dead time	200 ns

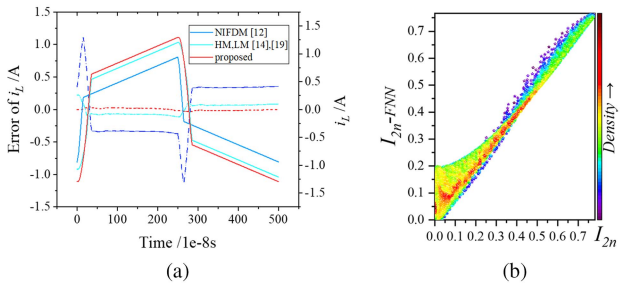

(a) (b)

Fig. 10. Model accuracy. (a) Accuracy of inductor current i_L using different analytical models. (b) Accuracy of general AI model.

Finally, the previously mentioned static and dynamic ratios are implemented in the microcontroller, as shown in Fig. 7. This controller can generate optimal modulation strategies online, resulting in excellent steady-state efficiency and transient performance.

V. PARAMETER DESIGN OF THE PROPOSED AI MODEL AND CONTROLLER

A. Parameters of the General AI Model

To validate the precision of the numerical modeling approach and the general AI model, comprehensive experiments were conducted. The DAB parameters are listed in Table III.

Fig. 10(a) shows the comparison of different models. By accounting for high-order harmonics, the harmonic model (HM) in [19] closely matches the piecewise linear model in [14]. NIFDM denotes the nonideality inclusive frequency domain model in [12]. The numerical model proposed in this article was found to almost precisely match the actual simulation results obtained in MATLAB/Simulink. It is more accurate than the traditional harmonic analysis theory, along with lower computation burden and derivation complexity. The data acquisition speed of this method is more than 100 times faster than that of MATLAB/Simulink.

The parameter optimization methods for the general AI model and the ANN, as shown in Fig. 8, are identical. A large training dataset is initially constructed using numerical simulations and algorithmic optimization. The optimization process employs the mean squared error as the loss function and utilizes the Adam optimizer to adjust the network parameters. Notably, this process is completed within a matter of minutes. In addition, from Fig. 10(b), R^2 of the proposed general AI model is up to 0.99. Once D_1 is employed as the dynamic modulation variable, the connection weights between the eight input neurons and the single neuron in the hidden layer are 0.56, 0.59, −0.14, 1.22, 3.89, -0.94, -3.87, and 0.21, respectively, with the bias b_1 being -2.08. Apart from this, w_{21} is 1.04, and the bias b_2 is 0.078. This lightweight model is not only applicable to all switching modes, but can also simplify the design of nonlinear controllers.

In the proposed DAB prototype, the parasitic inductance L_d and resistance R_{eq} are minimal, with L_d configured as 20 nH and R_{eq} set to 0.3 Ω. However, the equivalent parasitic capacitance $C_{Q,\text{eq}}$ of the MOSFET may reach up to 500 pF, with the dead time set at 200 ns. Consequently, the accuracy of the general AI model will decrease at high operating frequencies. To address this issue, a new AI model will be trained for 200 kHz under specific system parameters, while maintaining the same model structure as before.

B. Optimal Phase Shift Ratios of Steady State

Fig. 11(a) and (b) shows the optimal steady-state strategy of D_2^* and D_f^* only considering ZVS constraint I_E. These optimal ratios exhibit a positive correlation with V_2^* and P^*. Testing reveals that for small parasitic capacitance ($k_{Coss} < 0.2$) and moderate switching frequencies ($f_s \leq 100$ kHz), an ANN with more than five hidden-layer neurons can accurately map the steady-state optimization strategy across most operating conditions.

The phase shift values comparison with existing TPS modulation schemes in [14] and [19] has already been presented in Fig. 11(c) and (d). Owing to the high operating frequency of the DAB converter and the large parasitic capacitance C_{oss} of the MOSFET in this work, the proposed modulation strategy shows significant differences from the traditional modulation methods. Therefore, when the parasitic capacitance and operating frequency are relatively high, the ANN should be trained with specific system parameters to ensure optimal modulation strategy.

Due to the outstanding global search capability and simple structure, heuristic algorithms are widely favored in solving nonconvex optimization problems. Fig. 11(e) demonstrates the performance comparison of simulated annealing algorithm, GA, PSO, and the proposed algorithm, when $V_1 = 255$ V and $V_2 = 100$ V. The execution time of the algorithms in scenario when $P = 500$ W is also listed in the figure. It can be found that the proposed algorithm not only exhibits excellent global search capabilities but also needs less execution time.

C. Parameters of Transient Controller

Determining control parameters is often a tough task. In this article, PSO algorithm is used to quickly optimize the control parameters through numerical simulation.

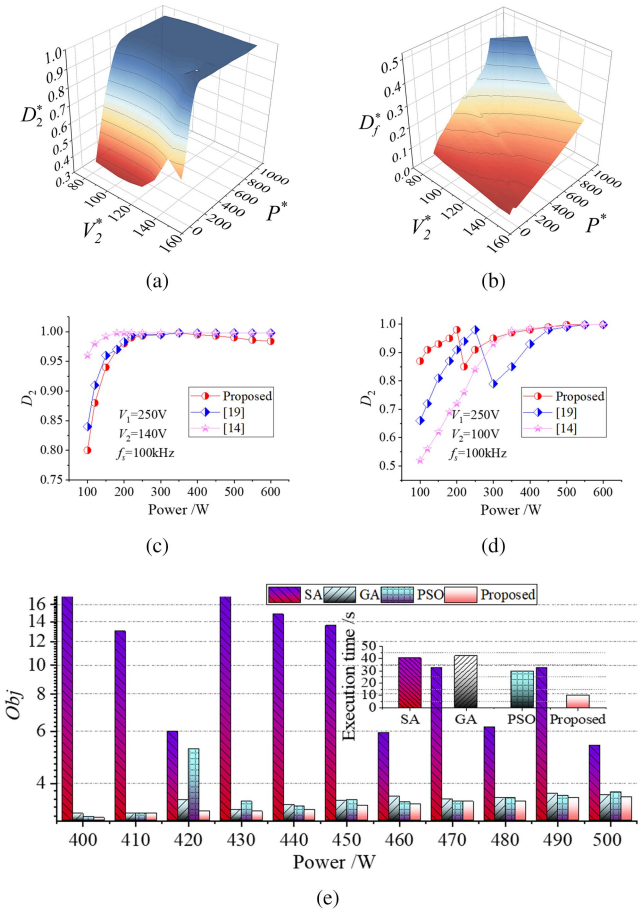

Fig. 11. Optimal modulation results of steady state. (a) Optimal phase shift ratio of D_2 only considering ZVS constraint I_E, when $V_1 = 255$ V, $V_2 = 100$ V, and $f_s = 100$ kHz. (b) Optimal phase shift ratio of D_2 only considering ZVS constraint I_E, when $V_1 = 255$ V, $V_2 = 100$ V, and $f_s = 100$ kHz. (c) Optimal phase shift ratio of D_2 considering the dynamic behavior of the circuit during the dead-time, when $V_1 = 250$ V, $V_2 = 140$ V, and $f_s = 100$ kHz. (d) Optimal phase shift ratio of D_2 considering the dynamic behavior of the circuit during the dead-time, when $V_1 = 250$ V, $V_2 = 100$ V, and $f_s = 100$ kHz. (e) Performance comparison of different heuristic algorithms.

Before optimization, a numerical model was constructed mirroring the circuit and control system, as described in Fig. 7. The objective Loss($\boldsymbol{\Theta}$) is to minimize the tracking error of the output voltage $|V_2^* - V_2|$ under various transient conditions. The control parameters $\{\kappa_1, \kappa_2, \delta_1, \delta_2, \delta_3, \eta\}$ of SMC and $\{W_z, \theta, b_z, W_h\}$ of RNN are treated as variables to be optimized, donated as $\boldsymbol{\Theta}$. Then, we employ PSO to solve the nonconvex problem

$$\text{Loss}\left(\boldsymbol{\Theta}\right) = \sum_{l=1}^{N_{p2}} \sum_{k=n_{p1}}^{N_{p1}} \left|V_2^*\left[k\right] - V_2\left[k\right]\right| \tag{41}$$

where N_{p1} is the time sequence of one scenario, and there are N_{p2} scenarios in total. The initial value of k is set to n_{p_1}, to pay more attention to the performance near the steady state. $\boldsymbol{Vel}_i$ represents the update velocity of the particle.

Through this approach, preliminary parameters of the proposed controller can be rapidly acquired without any theoretical derivation. Finally, we implement these parameters into the prototype. The initial control parameters through PSO optimization have already demonstrated good performance in practice. The final optimal control parameters can be obtained by fine-tuning, as shown in Table IV.

TABLE IV
PARAMETERS OF PROPOSED TRANSIENT CONTROLLER

Parameter of SMC	Value	Parameter of δV	Value
$\kappa_1(D_1)$ 100 kHz	1.7	$W_h(D_1)$ 100 kHz	291.5
$\kappa_1(D_f)$ 100 kHz	1.7	$W_h(D_f)$ 100 kHz	607.3
$\kappa_1(D_1)$ 200 kHz	0.85	$W_h(D_1)$ 200 kHz	291.5
$\kappa_1(D_f)$ 200 kHz	1.3	$W_h(D_f)$ 200 kHz	874.5
κ_2	0.07	θ	3
δ_1	8e3	b_z	3
δ_2	160	W_z	−0.024
δ_3	1e6	$eV_{\min}$	5

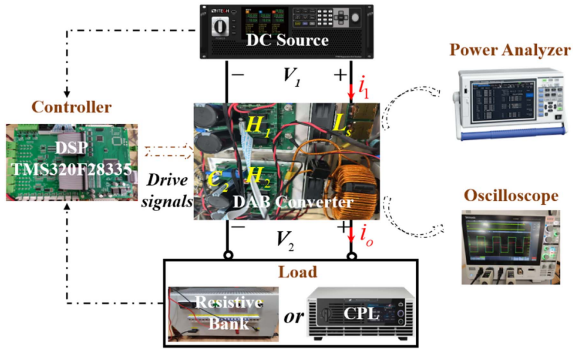

Fig. 12. Experimental platform of DAB converter.

VI. EXPERIMENTAL VERIFICATION

This section presents detailed experimental results concerning the model accuracy, steady state and transient performance of the proposed strategy. Apart from this, the tests of its robustness and computational burden are also conducted. A DAB converter prototype has been constructed to validate the effectiveness of the control algorithm. Its primary parameters are shown in Table III. Besides, the microprocessor is DSP-TMS320F28335. The control frequency is set to 10 kHz. Fig. 12 illustrates the framework of the experimental platform.

A. Experimental Results of Model Accuracy

The dataset for the proposed AI model is primarily derived from numerical simulation models, making the accuracy of the model critical to the precision of both steady-state and transient control strategies. Therefore, the accuracy of i_L, v_{ab}, v'_{cd}, P, and $i_{L\text{rms}}$ derived from the proposed model will be evaluated.

Fig. 13 shows the accuracy of inductor current i_L, v_{ab}, and v'_{cd} under different models. It is observed that the HM in [19] does not account for nonideal factors, such as parasitic parameters and dead-time effects, leading to significant deviations between the simulated and experimental i_L waveforms. Consequently, using i_L derived from the HM to assess the ZVS condition lacks accuracy. In contrast, the proposed numerical model accurately

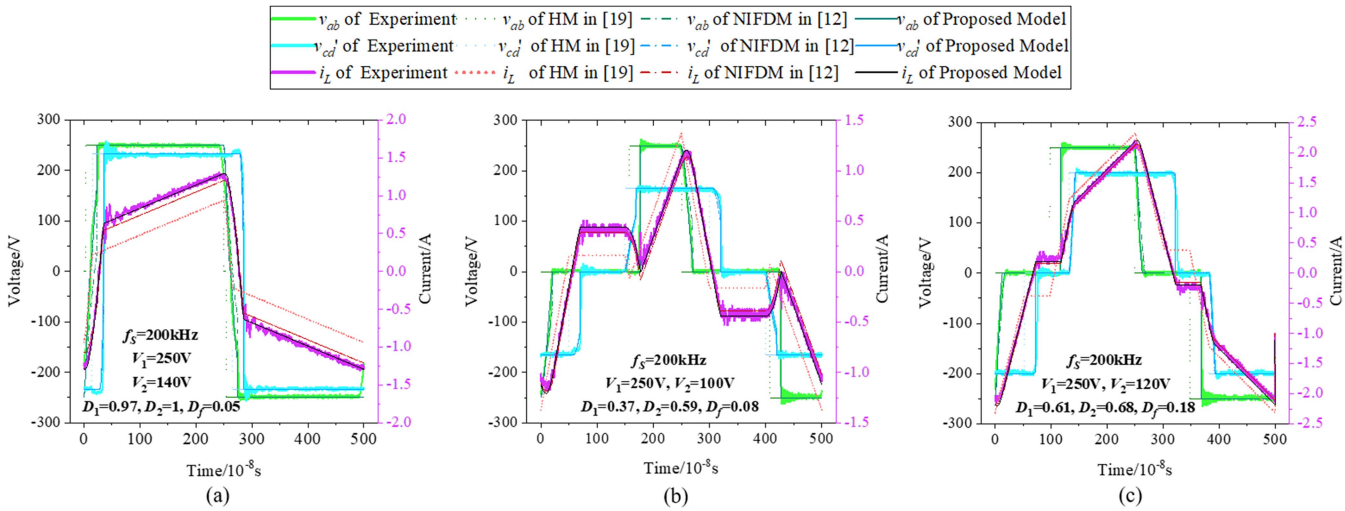

Fig. 13. Accuracy of inductor current i_L, v_{ab}, and v'_{cd} under different models. (a) $V_1 = 250$ V, $V_2 = 140$ V, $f_s = 200$ kHz, $D_1 = 0.97$, $D_2 = 1$, and $D_3 = 0.05$. (b) $V_1 = 250$ V, $V_2 = 100$ V, $f_s = 200$ kHz, $D_1 = 0.37$, $D_2 = 0.59$, and $D_3 = 0.08$. (c) $V_1 = 250$ V, $V_2 = 120$ V, $f_s = 200$ kHz, $D_1 = 0.61$, $D_2 = 0.68$, and $D_3 = 0.18$.

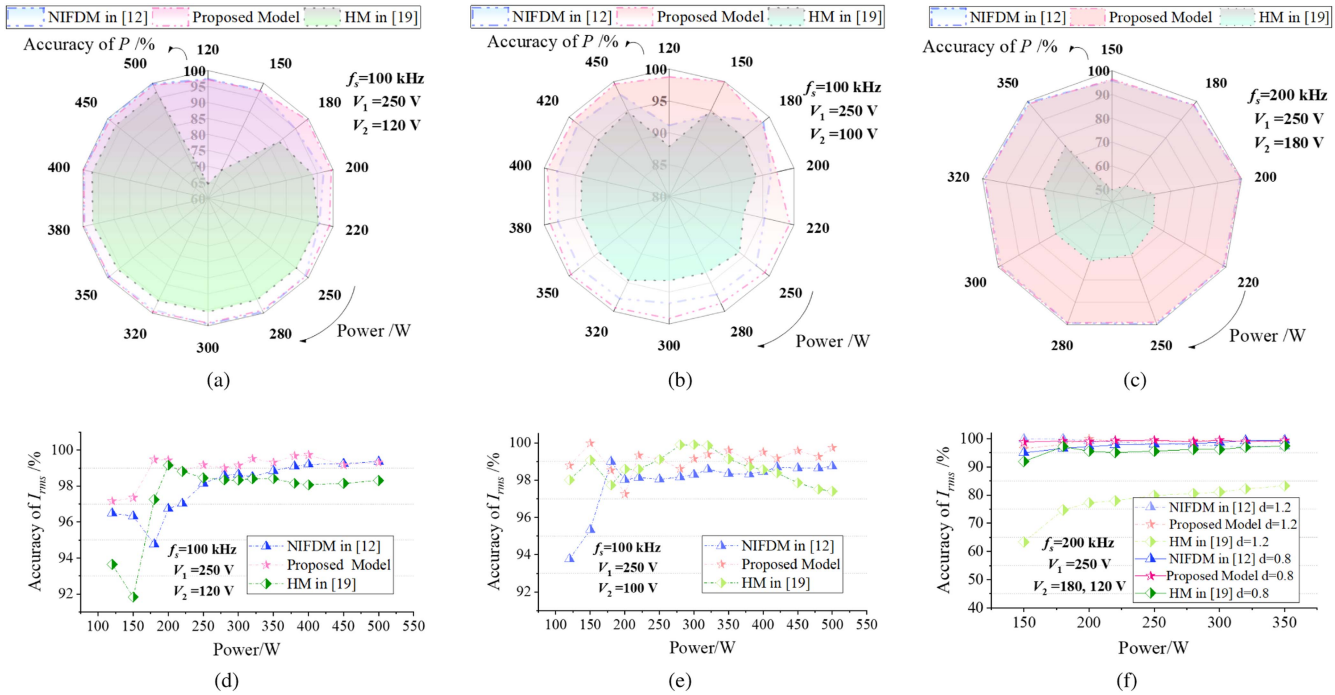

Fig. 14. Accuracy of transmission power P and i_{Lrms} under different models. (a) Accuracy of P, when $V_1 = 250$ V, $V_2 = 120$ V, and $f_s = 100$ kHz. (b) Accuracy of P, when $V_1 = 250$ V, $V_2 = 100$ V, and $f_s = 100$ kHz. (c) Accuracy of P, when $V_1 = 250$ V, $V_2 = 180$ V, and $f_s = 200$ kHz. (d) Accuracy of i_{Lrms}, when $V_1 = 250$ V, $V_2 = 120$ V, and $f_s = 100$ kHz. (e) Accuracy of i_{Lrms}, when $V_1 = 250$ V, $V_2 = 100$ V, and $f_s = 200$ kHz. (f) Accuracy of i_{Lrms}, when $V_1 = 250$ V, $V_2 = 180$ V or 120 V, and $f_s = 200$ kHz.

captures the dynamic behavior of the circuit, particularly during the dead time. Because the NIFDM in [12] employs some approximations for DAB circuit, leading to deviations from the experimental waveforms at certain nodes.

Meanwhile, the precision of transmission power P and i_{Lrms} under different models is also tested, as depicted in Fig. 14. The proposed numerical model demonstrates high predictive accuracy for P and i_{Lrms} under two operating frequencies. The predictive accuracy of the NIFDM model improves as P increases. Although the predictive accuracy of the HM exceeds 90% at 100 kHz, it declines rapidly at 200 kHz, especially when $d = 1.2$.

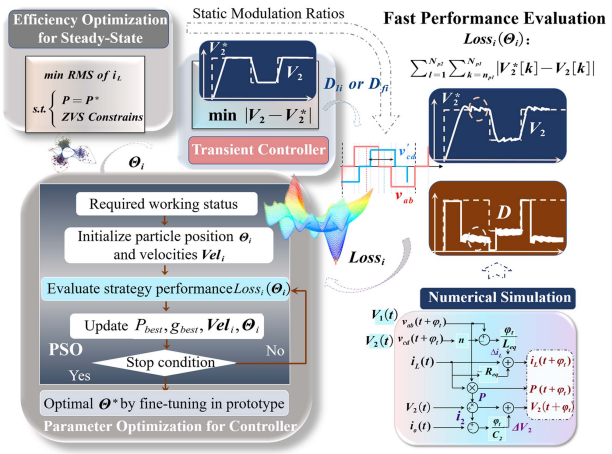

Fig. 15. Optimization process of transient control parameters.

B. Experimental Results of Steady State

The modulation strategy in this article is derived from a unified analysis of TPS. Thus, the proposed modulation will be described as unified triple phase shift modulation (UTPS) [41] in the following text.

To evaluate the steady-state performance of the proposed control strategy under different operating conditions, four scenarios are designed: Condition A, $V_1 = 250$ V, $V_2 = 140$ V, $d = 0.93$, and $f_s = 100$ kHz; Condition B, $V_1 = 250$ V, $V_2 = 100$ V, $d = 0.67$, and $f_s = 100$ kHz; Condition C, $V_1 = 250$ V, $V_2 = 140$ V, $d = 0.93$, and $f_s = 200$ kHz; Condition D, $V_1 = 250$ V, $V_2 = 100$ V, $d = 0.67$, and $f_s = 200$ kHz

To verify the effectiveness of the proposed strategy, TPS modulation strategies targeting i_{Lrms} optimization, as described in [14], [15], and [19], are adopted for comparison. In addition, three transient control methods are also set up for comparison: PI control under UTPS modulation (UTPS-PI), MPC under UTPS modulation (UTPS-MPC), and RNN control under UTPS modulation (UTPS-RNN). To balance steady-state efficiency and transient performance, the proportional coefficient and the integral coefficient of PI control are selected as 0.08 and 5 after fine-tuning in the prototype, respectively. Apart from this, the transient modulation strategy for UTPS-MPC is formulated with the same control objective as the proposed method. Using the general AI model and convex theory, the optimal dynamic phase shift ratio of UTPS-MPC can be obtained. The parameter optimization method for UTPS-RNN is consistent with proposed controller, as shown in Fig. 15.

Figs. 16–18 illustrate the soft switching performance of proposed strategy and TPS modulation schemes in [14], [15], and [19]. At relatively high frequencies, traditional methods will fail to ensure ZVS, and excessively increasing the dead time to extend the ZVS range may degrade the efficiency of the DAB converter under heavy loads. Therefore, the modulation strategy need to balance i_{Lrms} and the number of switches achieving ZVS with minimal dead time. It is observed that all switches in the proposed strategy achieve ZVS in Fig. 16, with a minor increase in i_{Lrms}. Under Condition C in Fig. 17, only two switches in other TPS modulation schemes achieve ZVS, whereas the proposed method enables six switches to achieve ZVS, with nearly identical i_{Lrms}.

Efficiency is another key indicator when evaluating the performance of a controller. Fig. 19 displays the efficiency and i_{Lrms} curves of steady state. When calculating the efficiency of the steady-state optimization strategies of TPS in [19], the transient control strategy is kept the same as the method proposed in this article. From Fig. 19(a) and (b), it can be observed that under Condition A, the efficiency under proposed method exceeds other modulations in the whole load range. As illustrated in Fig. 11, this is attributed to the ability of the proposed method to more effectively identify the modulation strategy that minimizes i_{Lrms} while maximizing the number of switches that satisfy the ZVS constraint. Specifically, the efficiency of the proposed method reaches 98.4% when $P = 450$ W. Furthermore, a comparison of efficiency curves reveals that SPS strategy based on the proposed transient control method (abbreviated as AIC) achieves higher operational efficiency than PI control, whereas MPC and RNN exhibit poor performance under Condition A.

From Fig. 19(b) and (e), the efficiency gap between the proposed UTPS control and other steady-state strategies becomes more pronounced at a voltage gain of 0.67. Hence, it can be concluded that, under various operating conditions, the proposed control strategy exhibits superior operating efficiency compared to other methods, especially when the converter is operated at low loads with a voltage gain far away from unity.

Fig. 19(c) and (f) illustrates the efficiency and i_{Lrms} curves at 200 kHz. The proposed strategy still achieves lower i_{Lrms} and higher efficiency. At 200 kHz, a longer dead time hinders DAB operation under light load conditions; thus, the dead time is fixed at 200 ns in this experiment. This limitation prevents the SPS strategy from achieving ZVS for all switches under heavy-load conditions with $d = 0.93$, leading to reduced efficiency.

C. Experimental Results of Transient Performance

Transient performance tests are conducted using both resistive and constant power loads. UTPS-PI, UPTS-MPC, and UTPS-RNN control strategies are investigated.

Fig. 20 shows the transient response of DAB with the increase and decrease of the load power, $V_1 = 200$ V, $V_2 = 150$ V, and $f_s = 100$ kHz. t_{r1} indicates the moment when the load resistance changes from 55.6 to 100 Ω. t_{r2} represents the opposite change. In this scenario, the output voltage overshoot of the proposed control strategy is 1.6 V as the load decreases. The settling time is only 13.6 ms, with nearly no undershoot when the load increases. In contrast, under UTPS-PI control, the dynamic overshoot and settling time is greater. Although the UTPS-MPC strategy does not exhibit any dynamic overshoot, its output voltage tracking error is 4.1 V. Meanwhile, the UTPS-RNN method demonstrates a 2 V overshoot and a 1.7 V steady-state error. Compared to other model-free controllers, model-based controllers typically exhibit better dynamic performance and reduced ripple.

Furthermore, the transient response of changing V_1 and V_2^* is tested, as shown in Fig. 21. Here, DAB feeds a constant power load (CPL), $V_1 = 150$ V, $f_s = 100$ kHz, and $P = 100$ W. In this scenario, t_{c1} marks the moment when the soft start is over

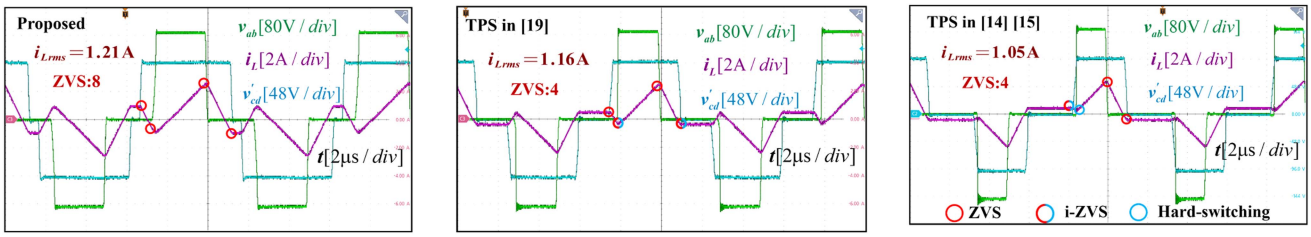

(a) (b) (c)

Fig. 16. Soft switching performance under Condition B, $V_1 = 250$ V, $V_2 = 100$ V, $f_s = 100$ kHz, and $P = 100$ W. (a) Proposed. (b) TPS in [19]. (c) TPS in [14] and [15].

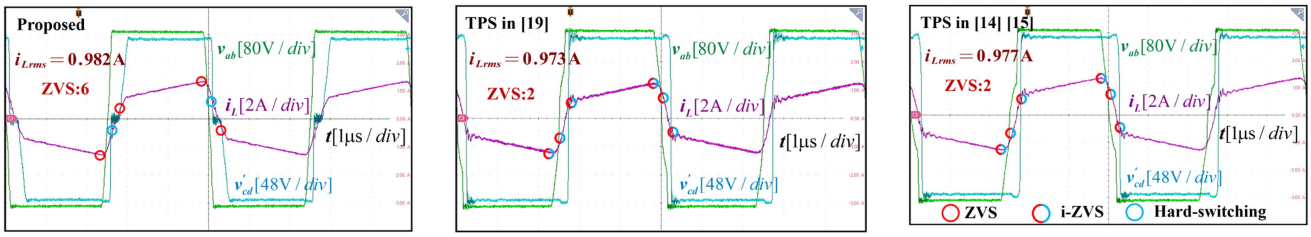

(a) (b) (c)

Fig. 17. Soft switching performance under Condition C, $V_1 = 250$ V, $V_2 = 140$ V, $f_s = 200$ kHz, and $P = 200$ W. (a) Proposed. (b) TPS in [19]. (c) TPS in [14] and [15].

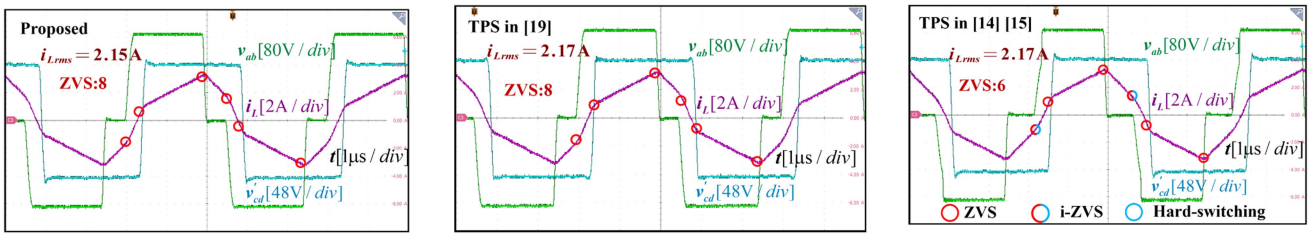

(a) (b) (c)

Fig. 18. Soft switching performance under Condition D, $V_1 = 250$ V, $V_2 = 100$ V, $f_s = 200$ kHz, and $P = 320$ W. (a) Proposed. (b) TPS in [19]. (c) TPS in [14] and [15].

and the device enters a constant current mode; t_{c2} is the end of current limitation; at t_{c3}, V_2^* changes from 100 to 60 V; it switches back at t_{c4}; and the input voltage V_1 steps up from 150 to 220 V at t_{c5}.

From Fig. 21, the proposed control strategy maintains excellent transient performance under complex disturbances. It almost has no overshoot or output voltage tracking error. In contrast, the PI control shows great dynamic overshoots and long settling time. The voltage overshoot even reaches 24.1 V after soft start. Meanwhile, the MPC still presents a slight output voltage tracking error, while the RNN demonstrates small overshoot.

With the aim of evaluating the impact of evolving the adaptive error compensation term δV on transient performance, Fig. 22 illustrates the transient response of DAB feeding CPL, with and without the compensation term when $V_1 = 250$ V, $f_s = 100$ kHz, and $V_2 = 100$ V. The power of CPL alternates between 100 and 300 W.

From Fig. 22, it can be found that when the load is suddenly increased, the SMC strategy without δV exhibits an output voltage tracking error of 1.2 V. In contrast, after adding δV, the error is eliminated, and the dynamic overshoot is nearly zero. This shows that the addition of δV can accelerate the convergence speed of the output voltage near the equilibrium state while minimizing dynamic overshoot.

In summary, the proposed strategy exhibits faster convergence and lower voltage overshoot than the PI controller. In addition, it enhances transient response compared to conventional SMC and RNN controllers, while achieving higher tracking accuracy than MPC.

D. Robustness and Computational Burden

To further validate the robustness of the control strategy, the impact of circuit parameter mismatches (L_s, C_2) on the control performance has also been tested.

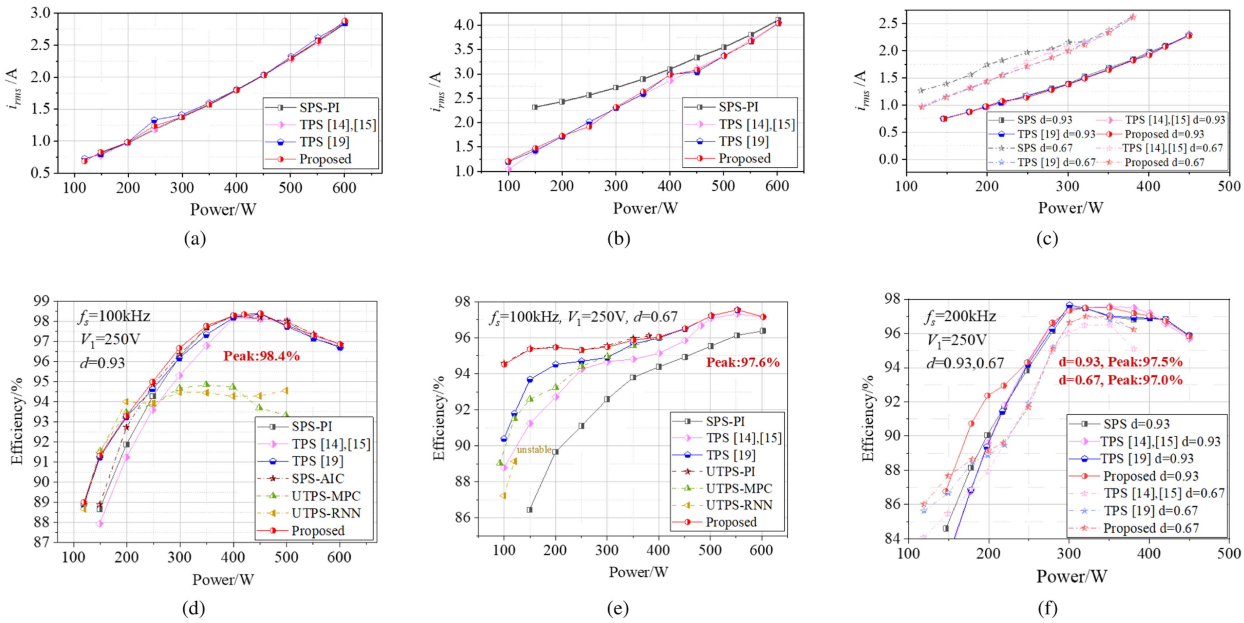

Fig. 19. Efficiency and $i_{L\text{rms}}$ of steady state under different operating conditions. (a) $i_{L\text{rms}}$ when $V_1 = 250$ V, $V_2 = 140$ V, $d = 0.93$, $f_s = 100$ kHz. (b) $i_{L\text{rms}}$ when $V_1 = 250$ V, $V_2 = 100$ V, $d = 0.67$, and $f_s = 100$ kHz. (c) $i_{L\text{rms}}$ when $V_1 = 250$ V, $V_2 = 140$ V or 100 V, $d = 0.93$ or 0.67, and $f_s = 200$ kHz. (d) Efficiency when $V_1 = 250$ V, $V_2 = 140$ V, $d = 0.93$, and $f_s = 100$ kHz. (e) Efficiency when $V_1 = 250$ V, $V_2 = 100$ V, $d = 0.67$, and $f_s = 100$ kHz. (f) Efficiency when $V_1 = 250$ V, $V_2 = 140$ V or 100 V, $d = 0.93$ or 0.67, and $f_s = 200$ kHz.

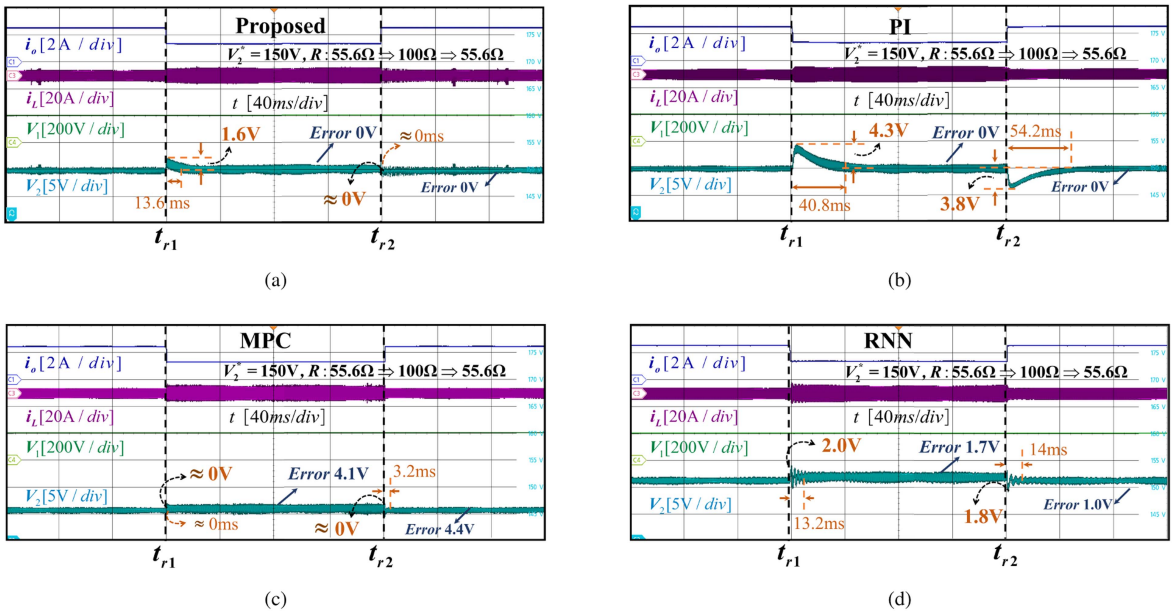

Fig. 20. DAB transient performance under load switching of resistor bank. (a) Proposed. (b) UTPS-PI. (c) UTPS-MPC. (d) UTPS-RNN.

Table V presents the transient response of the output voltage under various disturbances. The tests in Table V reveal that circuit parameter mismatches have a very small effect on the overshoot and tracking error of the output voltage.

Apart from these, performance under control parameter mismatch is also assessed. In response to changes within ±30% of κ_1 and κ_2 in the SMC, the steady-state efficiency exhibits fluctuations of approximately ±0.5%, and the convergence speed around the equilibrium point will be slightly affected. Other parameters, when varied within ± 30%, exhibit a relatively minor impact on the steady-state efficiency and transient performance of the system.

Considering the computational capabilities of conventional microprocessors, a test was conducted to evaluate the computational burden of the proposed control strategy. The execution time of the general AI model within microprocessor is less than 6 μs when using the DSP-TMS320F28335 with 150 MHz core frequency. Since the AI method used in the control strategy is lightweight, the timings for the transient controller are

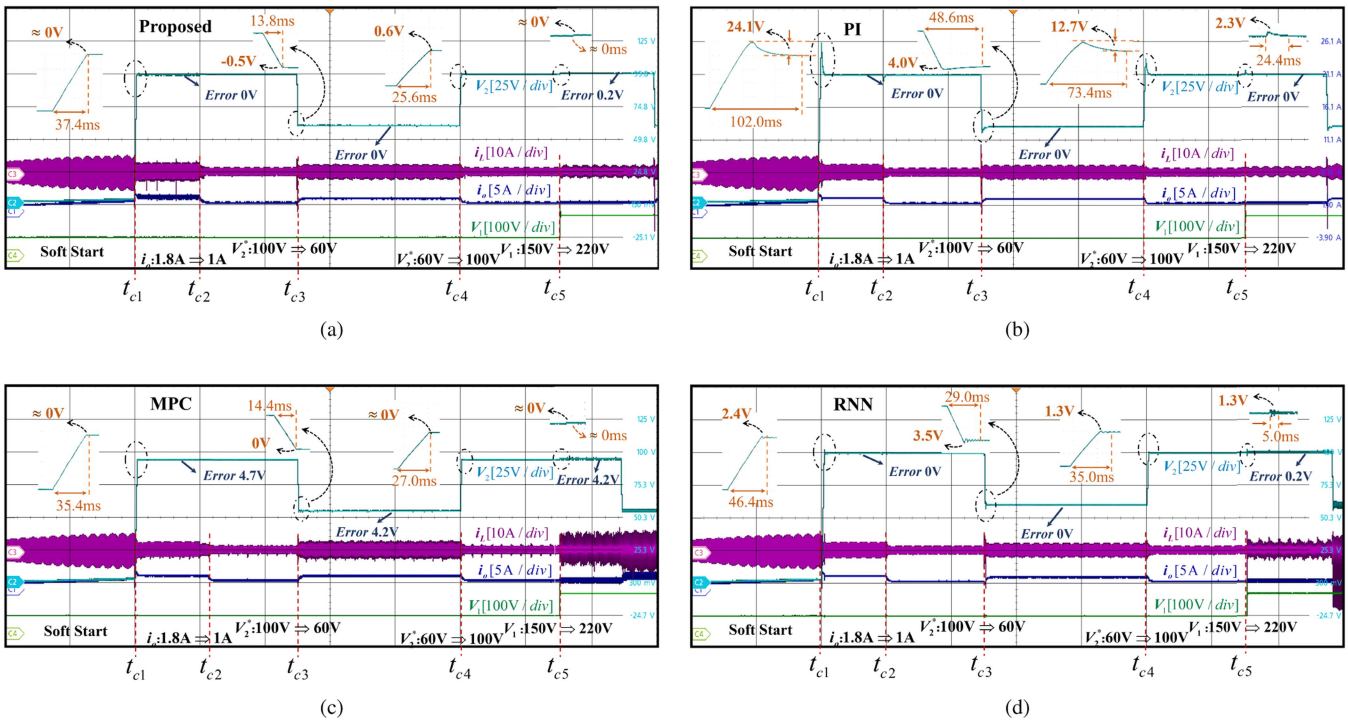

Fig. 21. Transient performance of DAB converter feeding CPL. (a) Proposed. (b) UTPS-PI. (c) UTPS-MPC. (d) UTPS-RNN.

TABLE V
TRANSIENT PERFORMANCE AND EXECUTION TIME OF DIFFERENT CONTROL STRATEGIES FOR DAB CONVERTER WITH TPS MODULATION

Method	Execution Time	Frequency	Scenarios	Overshoot	Settling Time	Steady-state Erro
Proposed	12.8 μs	100 kHz	$R: 100\ \Omega \Rightarrow 55.6\ \Omega, V_1 = 200\ \text{V}, V_2 = 150\ \text{V}$	0 V	0 ms	0 V
			$R: 100\ \Omega \Rightarrow 166.7\ \Omega, V_1 = 200\ \text{V}, V_2 = 110\ \text{V}$	0 V	0 ms	0.3 V
			$V_1: 150\ \text{V} \Rightarrow 220\ \text{V}, V_2^* = 100\ \text{V}, P = 100\ \text{W}$	0 V	0 ms	0.2 V
			$V_2^*: 60\ \text{V} \Rightarrow 100\ \text{V}, V_1 = 150\ \text{V}, P = 100\ \text{W}$	0.6 V	25.6 ms	0 V
			$i_o: 1.8\ \text{A} \Rightarrow 1.0\ \text{A}, V_1 = 150\ \text{V}, V_2^* = 100\ \text{V}$	0 V	0 ms	0 V
			$P: 100\ \text{W} \Rightarrow 300\ \text{W}, V_1 = 250\ \text{V}, V_2^* = 100\ \text{V}$	0 V	61.8 ms	0 V
			$P: 100\ \text{W} \Rightarrow 300\ \text{W}, V_1 = 250\ \text{V}, V_2^* = 100\ \text{V}$ $-30\%\ L_{eq}$	0 V	65.4 ms	0.3 V
			$P: 100\ \text{W} \Rightarrow 300\ \text{W}, V_1 = 250\ \text{V}, V_2^* = 100\ \text{V}$ $-30\%\ C_2$	0 V	67.1 ms	0.3 V
			$P: 100\ \text{W} \Rightarrow 300\ \text{W}, V_1 = 250\ \text{V}, V_2^* = 100\ \text{V}$ $+30\%\ L_{eq}$	0 V	59.2 ms	0 V
		200 kHz	$R: 166.7\ \Omega \Rightarrow 100\ \Omega, V_1 = 200\ \text{V}, V_2 = 150\ \text{V}$	0 V	0 ms	0 V
			$R: 166.7\ \Omega \Rightarrow 100\ \Omega, V_1 = 200\ \text{V}, V_2 = 110\ \text{V}$	0 V	0 ms	0.3 V
			$V_1: 150\ \text{V} \Rightarrow 220\ \text{V}, V_2^* = 100\ \text{V}, P = 100\ \text{W}$	0.3 V	3.4 ms	0.5 V
			$V_2^*: 60\ \text{V} \Rightarrow 100\ \text{V}, V_1 = 150\ \text{V}, P = 100\ \text{W}$	0.7 V	46.2 ms	0 V
PI	0.8 μs	100 kHz	$R: 100\Omega \Rightarrow 166.7\ \Omega, V_1 = 200\ \text{V}, V_2 = 110\ \text{V}$	3.8 V	54.2 ms	0 V
			$V_1: 150\text{V} \Rightarrow 220\ \text{V}, V_2^* = 100\ \text{V}, P = 100\ \text{W}$	2.3 V	24.4 ms	0 V
			$V_2^*: 60\text{V} \Rightarrow 100\ \text{V}, V_1 = 150\ \text{V}, P = 100\ \text{W}$	12.7 V	73.4 ms	0 V
			$i_o: 1.8\text{A} \Rightarrow 1.0\ \text{A}, V_1 = 150\ \text{V}, V_2^* = 100\ \text{V}$	3.2 V	30.2 ms	0 V
MPC	17.4 μs	100 kHz	$R: 100\ \Omega \Rightarrow 166.7\ \Omega, V_1 = 200\ \text{V}, V_2 = 110\ \text{V}$	0 V	0 ms	4.4 V
			$V_1: 150\ \text{V} \Rightarrow 220\ \text{V}, V_2^* = 100\ \text{V}, P = 100\ \text{W}$	0 V	0 ms	4.2 V
			$V_2^*: 60\ \text{V} \Rightarrow 100\ \text{V}, V_1 = 150\ \text{V}, P = 100\ \text{W}$	0 V	0 ms	4.7 V
			$i_o: 1.8\ \text{A} \Rightarrow 1.0\ \text{A}, V_1 = 150\ \text{V}, V_2^* = 100\ \text{V}$	0 V	0 ms	4.7 V
RNN	33.6 μs	100 kHz	$R: 100\ \Omega \Rightarrow 166.7\ \Omega, V_1 = 200\ \text{V}, V_2 = 110\ \text{V}$	1.8 V	14 ms	1.0 V
			$V_1: 150\ \text{V} \Rightarrow 220\ \text{V}, V_2^* = 100\ \text{V}, P = 100\ \text{W}$	1.3 V	5.0 ms	0.2 V
			$V_2^*: 60\ \text{V} \Rightarrow 100\ \text{V}, V_1 = 150\ \text{V}, P = 100\ \text{W}$	1.3 V	35.0 ms	0 V
			$i_o: 1.8\ \text{A} \Rightarrow 1.0\ \text{A}, V_1 = 150\ \text{V}, V_2^* = 100\ \text{V}$	0 V	0 ms	0 V

less than 13 μs. Table V summarizes the transient performance and execution time of various control strategies applied to the DAB converter with TPS modulation. The experimental results indicate that the proposed AI-based control strategy achieves superior dynamic performance while maintaining a low computational burden.

Table VI presents an overview of some key features of the proposed control strategy and other existing transient control methods, including theoretical derivation complexity, transient performance, robustness, and implementation costs. In conclusion, the proposed method outperforms other controllers in many aspects.

TABLE VI
COMPARISON OF DAB TRANSIENT CONTROL STRATEGIES

Method	Theoretical complexity	Transient performance	Steady-state error	Robustness	Computational complexity	Number of sensors
Proposed	Medium	++++	Nearly zero	++++	Medium	1
UTPS-PI	Low	++	Nearly zero	++	Low	1
UTPS-SMC	Medium	+++	Small	+++	Medium	2
UTPS-RNN	Medium	+++	Small	*	Medium-High	1
Normal MPC	High	+++	Small	++	Medium	2
TPS-MPC [28]	High	+++	Nearly zero	*	Medium	3
SPS-DRL [33]	Medium	+++	Small	*	High	2

Note: +=Poor; ++=Average; +++=Good; ++++=Excellent; *=Unknown.

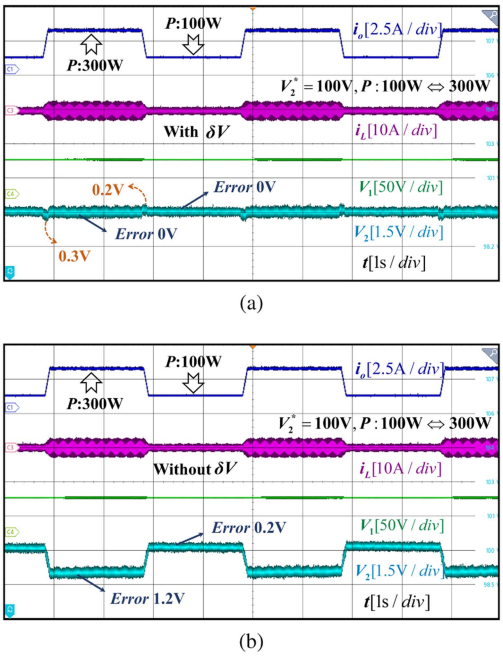

Fig. 22. Improvement of system transient performance due to the adaptive error compensation δV based on RNN when feeding CPL. (a) with δV. (b) without δV.

VII. CONCLUSION

This article proposes an AI-based modeling and control strategy for DAB converter with TPS modulation. Such approach can achieve an enhancement of steady-state and transient performance simultaneously. The establishment of the general AI model simplifies the design of nonlinear control strategies with TPS modulation. Furthermore, due to the integration of SMC theory with the adaptive error compensation term based on RNN, the proposed control strategy demonstrates excellent transient performance and robustness against disturbances, including load variations, input voltage fluctuations, changes in reference output voltage, and parameter mismatches. Experimental results validate the superior steady-state and transient performance of the proposed strategy. Comparisons with other control methods further demonstrate their advantages in terms of theoretical complexity, efficiency, transient performance, and implementation costs. Therefore, the research presented holds significant promise for applications in dc converter control. It offers valuable guidance in constructing models of nonlinear elements and designing robust control strategies.

REFERENCES

[1] S. Kaler and A. Yazdani, "An isolated modular multiport converter for the integration of photovoltaic energy sources and battery storage in MVDC networks," *IEEE Trans. Energy Convers.*, early access, Jan. 17, 2025, doi: 10.1109/TEC.2024.3488598.
[2] Y. Wu, X. Pan, L. Yang, H. Yuan, and Z. Cai, "Asymmetric phase shift control in multiphase dual active bridge DC/DC converters," *IEEE J. Emerg. Sel. Topics Ind. Electron.*, early access, Jan. 20, 2025, doi: 10.1109/JESTIE.2025.3531358.
[3] X. Chen, G. Xu, H. Han, D. Liu, Y. Sun, and M. Su, "Light-load efficiency enhancement of high-frequency dual-active-bridge converter under SPS control," *IEEE Trans. Ind. Electron.*, vol. 68, no. 12, pp. 12941–12946, Dec. 2021.
[4] G. Xu, M. Zhang, X. Chen, L. Li, Z. Lu, and M. Su, "Dual-coupled-inductor-based DAB DCX converter with full load range ZVs," *IEEE Trans. Ind. Electron.*, vol. 72, no. 1, pp. 525–535, Jan. 2025.
[5] F. Wu, F. Feng, and H. B. Gooi, "Cooperative triple-phase-shift control for isolated DAB DC–DC converter to improve current characteristics," *IEEE Trans. Ind. Electron.*, vol. 66, no. 9, pp. 7022–7031, Sep. 2019.
[6] S. Shao, M. Jiang, W. Ye, Y. Li, J. Zhang, and K. Sheng, "Optimal phase-shift control to minimize reactive power for a dual active bridge DC–DC converter," *IEEE Trans. Power Electron.*, vol. 34, no. 10, pp. 10193–10205, Oct. 2019.
[7] B. Zhao, Q. Song, W. Liu, G. Liu, and Y. Zhao, "Universal high-frequency-link characterization and practical fundamental-optimal strategy for dual-active-bridge DC-DC converter under PWM plus phase-shift control," *IEEE Trans. Power Electron.*, vol. 30, no. 12, pp. 6488–6494, Dec. 2015.
[8] H. Shi, H. Wen, J. Chen, Y. Hu, L. Jiang, and G. Chen, "Minimum-reactive-power scheme of dual-active-bridge DC–DC converter with three-level modulated phase-shift control," *IEEE Trans. Ind. Appl.*, vol. 53, no. 6, pp. 5573–5586, Nov./Dec. 2017.
[9] S. Subedi, Y. Gui, and Y. Xue, "Applications of data-driven dynamic modeling of power converters in power systems: An overview," *IEEE Trans. Ind. Appl.*, vol. 61, no. 2, pp. 2434–2456, Mar./Apr. 2025, doi: 10.1109/TIA.2025.3529797.
[10] X. Li, F. Lin, X. Zhang, H. Ma, and F. Blaabjerg, "Data-light physics-informed modeling for the modulation optimization of a dual-active-bridge converter," *IEEE Trans. Power Electron.*, vol. 39, no. 7, pp. 8770–8785, Jul. 2024.
[11] F. Lin et al., "AI-based design with data trimming for hybrid phase shift modulation for minimum-current-stress dual active bridge converter," *IEEE J. Emerg. Sel. Topics Power Electron.*, vol. 12, no. 2, pp. 2268–2280, Apr. 2024.
[12] S. Dey and A. Mallik, "Physics informed neural network—Estimated circuit parameter adaptive modulation of DAB," *IEEE Trans. Power Electron.*, vol. 40, no. 10, pp. 14821–14841, Oct. 2025, doi: 10.1109/TPEL.2025.3574873.
[13] F. Krismer and J. W. Kolar, "Efficiency-optimized high-current dual active bridge converter for automotive applications," *IEEE Trans. Ind. Electron.*, vol. 59, no. 7, pp. 2745–2760, Jul. 2012.
[14] A. Tong, L. Hang, G. Li, X. Jiang, and S. Gao, "Modeling and analysis of a dual-active-bridge-isolated bidirectional DC/DC converter to minimize RMS current with whole operating range," *IEEE Trans. Power Electron.*, vol. 33, no. 6, pp. 5302–5316, Jun. 2018.
[15] H. Yu et al., "Globally unified ZVS and quasi-optimal minimum conduction loss modulation of DAB converters," *IEEE Trans. Transp. Electrif.*, vol. 8, no. 3, pp. 3989–4000, Sep. 2022.
[16] L. Gong et al., "A dynamic ZVS-guaranteed and seamless-mode-transition modulation scheme for the DAB converter that maximizes the ZVS range and lowers the inductor RMS current," *IEEE Trans. Power Electron.*, vol. 37, no. 11, pp. 13119–13134, Nov. 2022.

[17] S. Li, X. Yuan, Z. Wang, K. Wang, Y. Zhang, and X. Wu, "A unified optimal modulation strategy for DAB converters to tradeoff the backflow power reduction and all ZVS in the full operating range," *IEEE J. Emerg. Sel. Topics Power Electron.*, vol. 11, no. 6, pp. 5701–5723, Dec. 2023.
[18] X. Yang, J. Wang, Y. Du, C. Liu, T. Zhang, and J. Zhang, "Bidirectional ZVS operation of all switches for a DAB converter over a full range of loads with optimized current stress," *IEEE Trans. Ind. Appl.*, vol. 60, no. 1, pp. 1183–1195, Jan./Feb. 2024.
[19] G. Park, H. Kim, B.-G. Cho, and S. Cui, "ZVS-enhanced and RMS-current-minimized optimal modulation scheme of dual-active bridge converter with comprehensive ZVS analysis," *IEEE Trans. Power Electron.*, vol. 40, no. 7, pp. 9004–9018, Jul. 2025, doi: 10.1109/TPEL.2025.3541847.
[20] Y. Tang et al., "Rl-ann-based minimum-current-stress scheme for the dual-active-bridge converter with triple-phase-shift control," *IEEE J. Emerg. Sel. Topics Power Electron.*, vol. 10, no. 1, pp. 673–689, Feb. 2022.
[21] N. Vazquez and M. Liserre, "Peak current control and feed-forward compensation of a DAB converter," *IEEE Trans. Ind. Electron.*, vol. 67, no. 10, pp. 8381–8391, Oct. 2020.
[22] Y. Pan et al., "A dual-loop control to ensure fast and stable fault-tolerant operation of series resonant DAB converters," *IEEE Trans. Power Electron.*, vol. 35, no. 10, pp. 10994–11012, Oct. 2020.
[23] Z. Cao et al., "Constant power load stabilization with fast transient boundary control for DAB-converters-based electric drive systems," *IEEE Trans. Ind. Electron.*, vol. 71, no. 2, pp. 1863–1874, Feb. 2024.
[24] Y. Deng, W. Song, S. Yin, M. Zhong, K. Yang, and X. Feng, "A model predictive control scheme without current sensor of dual active bridge DC–DC converters: Improving dynamic performance and reducing hardware cost," *IEEE Trans. Transp. Electrif.*, vol. 9, no. 2, pp. 2916–2928, Jun. 2023.
[25] K. Yu, F. Zhuo, F. Wang, X. Jiang, and Y. Gou, "MPC-based startup current shaping strategy with state-space model of DAB in DC distribution system," *IEEE J. Emerg. Sel. Topics Power Electron.*, vol. 10, no. 4, pp. 4073–4089, Aug. 2022.
[26] N. Tiwary, V. Naik N, A. K. Panda, A. Narendra, and R. K. Lenka, "A robust voltage control of DAB converter with super-twisting sliding mode approach," *IEEE J. Emerg. Sel. Topics Ind. Electron.*, vol. 4, no. 1, pp. 288–298, Jan. 2023.
[27] Y.-C. Jeung and D.-C. Lee, "Voltage and current regulations of bidirectional isolated dual-active-bridge DC–DC converters based on a double-integral sliding mode control," *IEEE Trans. Power Electron.*, vol. 34, no. 7, pp. 6937–6946, Jul. 2019.
[28] D. Kong, X. Gao, Z. Zhang, C. Liu, M. L. Heldwein, and R. Kennel, "Minimization of current stress for dual active bridge converters based on model predictive control with enhanced ZVS ability," *IEEE Trans. Ind. Electron.*, vol. 71, no. 8, pp. 8970–8980, Aug. 2024.
[29] F. Lin et al., "Pe-GPT: A new paradigm for power electronics design," *IEEE Trans. Ind. Electron.*, vol. 72, no. 4, pp. 3778–3791, Apr. 2024, doi: 10.1109/TIE.2024.3454408.
[30] X. Li, X. Zhang, F. Lin, C. Sun, and K. Mao, "Artificial-intelligence-based triple phase shift modulation for dual active bridge converter with minimized current stress," *IEEE J. Emerg. Sel. Topics Power Electron.*, vol. 11, no. 4, pp. 4430–4441, Aug. 2023.
[31] Z. Xiao et al., "A hybrid data-driven power loss minimization method of dual-active bridge converters," *IEEE Trans. Power Electron.*, vol. 39, no. 5, pp. 5820–5832, May 2024.
[32] Y. Zeng et al., "Active disturbance rejection control using artificial neural network for dual-active-bridge-based energy storage system," *IEEE J. Emerg. Sel. Topics Power Electron.*, vol. 11, no. 1, pp. 301–311, Feb. 2023.
[33] X. Meng, Y. Jia, Q. Xu, C. Ren, X. Han, and P. Wang, "A novel intelligent nonlinear controller for dual active bridge converter with constant power loads," *IEEE Trans. Ind. Electron.*, vol. 70, no. 3, pp. 2887–2896, Mar. 2023.
[34] Y. Zhang et al., "Deep reinforcement learning and deadbeat hybrid control method for hybrid energy storage system considering nonlinear power loss and model mismatch," *IEEE Trans. Ind. Informat.*, vol. 21, no. 4, pp. 3296–3305, Apr. 2025, doi: 10.1109/TII.2024.3523585.
[35] A. Merabet, S. Kanukollu, A. Al-Durra, and E. F. El-Saadany, "Adaptive recurrent neural network for uncertainties estimation in feedback control system," *J. Autom. Intell.*, vol. 2, no. 3, pp. 119–129, Aug. 2023.
[36] J. Fei and L. Liu, "Real-time nonlinear model predictive control of active power filter using self-feedback recurrent fuzzy neural network estimator," *IEEE Trans. Ind. Electron.*, vol. 69, no. 8, pp. 8366–8376, Aug. 2022.
[37] D. Zhao et al., "Improved active damping stabilization of DAB converter interfaced aircraft DC microgrids using neural network-based model predictive control," *IEEE Trans. Transp. Electrif.*, vol. 8, no. 2, pp. 1541–1552, Jun. 2022.
[38] L. Li, G. Xu, D. Sha, Y. Liu, Y. Sun, and M. Su, "Review of dual-active-bridge converters with topological modifications," *IEEE Trans. Power Electron.*, vol. 38, no. 7, pp. 9046–9076, Jul. 2023.
[39] M. Kasper, R. M. Burkart, G. Deboy, and J. W. Kolar, "ZVS of power mosfets revisited," *IEEE Trans. Power Electron.*, vol. 31, no. 12, pp. 8063–8067, Dec. 2016.
[40] Y. Tang et al., "Artificial intelligence-aided minimum reactive power control for the DAB converter based on harmonic analysis method," *IEEE Trans. Power Electron.*, vol. 36, no. 9, pp. 9704–9710, Sep. 2021.
[41] J. Huang, Y. Wang, Z. Li, and W. Lei, "Unified triple-phase-shift control to minimize current stress and achieve full soft-switching of isolated bidirectional DC–DC converter," *IEEE Trans. Ind. Electron.*, vol. 63, no. 7, pp. 4169–4179, Jul. 2016.

Jiawei Zhang received the B.S. degree in electrical engineering from Xi'an Jiaotong University, Xi'an, China, in 2023. She is currently working toward the M.S. degree in electrical engineering with the College of Electrical Engineering, Zhejiang University, Hangzhou, China.

Her research interests include artificial intelligence modeling and control of dc converters.

Jiaxiong Xu received the B.S. degree in automation in 2020 from the College of Electrical Engineering, Zhejiang University, Hangzhou, China, where he is currently working toward the Ph.D. degree in electrical engineering.

His current research interests include soft-switching techniques, modulation, and control of grid-tied inverters.

Yile Dai was born in Sichuan, China, in 2002. He received the B.S. degree in electrical engineering and automation from Beijing Jiaotong University, Beijing, China, in 2024. He is currently working toward the Ph.D. degree in electrical engineering with Zhejiang University, Hangzhou, China.

His research interests include control of grid-connected inverters, microgrids, and stability analysis of multiinverter systems.

Miao Yu (Member, IEEE) received the B.S. degree in automation and the Ph.D. degree in control science and engineering from the College of Electrical Engineering, Zhejiang University, Hangzhou, China, in 2007 and 2012, respectively.

From 2013 to 2015, he was a Postdoctoral Researcher with Aalto University, Espoo, Finland. He is currently a Professor with the College of Electrical Engineering, Zhejiang University. His current research interests include control strategies in microgrids and renewable power generation.

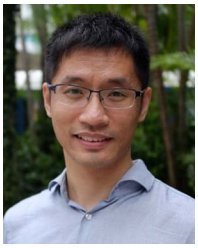

Xin Zhang (Senior Member, IEEE) received the Ph.D. degree in automatic control and systems engineering from the University of Sheffield, Sheffield, U.K., in 2016, and the Ph.D. degree in electronic and electrical engineering from the Nanjing University of Aeronautics and Astronautics, Nanjing, China, in 2014.

From 2017 to 2020, he was an Assistant Professor of power engineering with the School of Electrical and Electronic Engineering, Nanyang Technological University, Singapore. He is currently the Professor with Zhejiang University. His research interests include in power electronics, power systems, and advanced control theory, together with their applications in various sectors.

Huai Wang (Senior Member, IEEE) received the B.E. degree in electrical engineering from the Huazhong University of Science and Technology, Wuhan, China, in 2007, and the Ph.D. degree in power electronics from the City University of Hong Kong, Hong Kong, in 2012.

From August to September 2014, he was a Visiting Scientist with ETH Zürich, Zürich, Switzerland, and from September to November 2013, he was with the Massachusetts Institute of Technology, Cambridge, MA, USA. In 2009, he was with the ABB Corporate Research Center, Baden, Switzerland. He is currently a Professor with AAU Energy, Aalborg University, Aalborg, Denmark, where he leads the group of Reliability of Power Electronic Converters (ReliaPEC) and the mission on digital transformation and AI. His research interests include the fundamental challenges in modeling and validating power electronic component failure mechanisms and application issues in system-level predictability, condition monitoring, circuit architecture, and robustness design.